Carbon Doping and V-Pits in AlGaN/GaN HEMT Structures on Silicon

by

Maurits Verkerke

A thesis submitted in partial fulfillment for the
degree of Master of Science

at
Physics of Interfaces and Nanomaterials
Faculty of Science and Technology

October 2015

UNIVERSITY OF TWENTE. Fraunhofer
IAF

TWENTE UNIVERSITY

Abstract

Physics of Interfaces and Nanomaterials
Faculty of Science and Technology

Master of Science

by Maurits Verkerke

A high electron mobility transistor (HEMT) is a transistor with a channel with high electron mobility. An important performance characteristic of a gallium nitride (GaN) HEMT is its high breakdown voltage. To improve this voltage, the GaN (grown via metal-organic chemical vapor deposition) is doped with carbon atoms, yet this increases the density of V-pits, which lower the device quality. In order to restore low V-pit density, pentane is used as carbon source, allowing higher growth pressure. The effect of the growth parameters pressure and dopant type on the V-pit density and morphology are studied in this work, through examination of three species of samples: 1) low pressure samples with high carbon concentration through precursor doping, 2) high pressure samples with low (non-intentional) carbon concentration and 3) high pressure samples with high carbon concentration through pentane doping. Automated optical inspection and scanning electron microscopy are used to characterize the surface morphology of the samples. Transmission electron microscopy (TEM) is used to study the origin of the V-pit.

Increasing the pressure by 165 mbar and the surface temperature by 70°C) lowers the V-pit density by a factor 3±0.7. Adding pentane further decreases the density a factor 10±5. TEM measurements attribute the change in density to an increase in lateral growth of a factor 2.7±0.5 over 70°C and 165 mbar. Doping a sample with carbon increases the average pit diameter and pit depth by a factor 3.5±1.5. Using pentane as dopant changes the facet orientation of the V-pits from $\{1\bar{1}01\}$-planes to $\{11\bar{2}2\}$-planes. Based on these results a simple model for formation and closure of V-pits is proposed. This model states that V-pits originate when the vertical growth is disturbed. Growth parameters temperature, pressure and carbon concentration affect the lateral growth rate, which eventually can close the pit if it is high enough to overcome the disturbance.

Acknowledgements

Throughout the nine months I spent working on this thesis, I came to know a lot of people I owe my gratitude to.

Firstly I would like to thank Prof. Harold Zandvliet for the support and swift replies, even though I was most of the time far away in Freiburg.

Then I would like to thank the colleagues and staff of the Fraunhofer Institut für Angewandte Festkörperphysik in Freiburg for their hospitality towards a foreign student such as me, and for the very pleasant work environment they have created.

Of these colleagues I would like to my explicitly express sincere gratitude to Stefan Müller and Klaus Köhler for sharing their seemingly infinite wisdom in fruitful discussions.

Above all I am ultimately glad to have had such a wonderful supervisor as Steffen Breuer. It was a sincere pleasure working with you both in and out of the institute.

Contents

Abbreviations

2DEG	2-dimensional electron gas
3G/4G	third/fourth generation
A1	sample M0825-11 (low pressure, precursor doped)
A2	sample M0825-07 (low pressure, precursor doped)
AlGaAs	aluminum gallium arsenide
AlGaN	aluminum gallium nitride
AlN	aluminum nitride
$\mathbf{Al_2O_3}$	sapphire
AOI	automated optical inspection
B1	sample M0860-04 (high pressure, pentane doped)
B2	sample M0860-11 (high pressure, pentane doped)
CO	carbon monoxide
$\mathbf{CO_2}$	carbon dioxide
EDX	energy-dispersive X-ray spectroscopy
Fe	iron
FIB	focused ion beam
GaAs	gallium arsenide
$\mathbf{Ga(CH_3)_3}$	trimethyl gallium
GaN	gallium nitride
HEMT	high electron mobility transistor
HT	high temperature
IDB	inversion domain boundary
InN	indium nitride
LGR	lateral growth rate
LT	low temperature

MBE	molecular beam epitaxy
MOCVD	metal-organic chemical vapor deposition
MOVPE	metal-organic vapor phase epitaxy
NH_3	ammonia
n.i.d.	non-intentionally doped
R1	Sample M0830-02 (high pressure, non-intentionally doped)
R2	Sample M1007-06 (high pressure, non-intentionally doped)
SEM	scanning electron microscope
Si	silicon
SiC	silicon carbide
TEC	thermal expansion coefficient
TMA	trimethyl aluminum
TMG	trimethyl gallium
XRD	X-ray diffraction

Chapter 1

Introduction

High electron mobility transistors (HEMTs) made of gallium nitride (GaN) have attracted a lot of interest for applications in high power microwave device applications [1]. Typically these HEMTs are used in mobile base stations for 3G and 4G broadcasting [2]. The high band gap of GaN is the important parameter enabling high voltage application. An important characteristic of the HEMT in these high voltage applications is the breakdown voltage, the voltage at which the HEMT starts to degrade. Doping is applied in order to further increase the breakdown voltage. Iron is a popular and well-studied dopant, but is not applicable to silicon substrates, which for most applications is most favorable. For these silicon substrates carbon can be used as dopant, but its effect is less well-known. The introduction of carbon has been found to increase the breakdown voltage, but also introduces a decline in crystal quality and therefore overall performance of the HEMT. One particular problem is the high density of hexagonal V-pits as compared to iron-doped or non-intentionally doped GaN. A way to restore the crystal quality while doping with carbon has recently been established at the Fraunhofer Institute for Applied Solid State Physics (IAF); a different source of carbon (pentane) is used. The influence of using this pentane, and the higher growth pressure its use enables, on the density of V-pits is explored in this work. Additionally the influence of the growth pressure and pentane on the morphology of V-pits is considered, in order to try to understand in detail the mechanism involved in the formation of the V-pits.

In chapter 2 some fundamental aspects are covered, to provide an introduction into the phenomena and apparatuses concerned in these experiments. Firstly the properties of the materials used to build a HEMT are presented, after which the explanation of the principles of HEMTs naturally follow. The method of epitaxially growing layers by metal-organic chemical vapor deposition (MOCVD) is explained afterwards. Explicit details concerning the structures used in these experiments are saved for chapter 2, where they are directly applied to the experiments. In the remainder of chapter 1 typical crystalline defects are introduced and literature on hexagonal V-pits is discussed. Lastly the inspection tools used in this research are introduced.

In chapter 3 the measurements of V-pit densities are described. It starts off by treating the sample structure layer by layer. Some theoretical aspects are explained here to give grounds for the chosen structure. Then the difference between the samples that are used in these experiments is presented. Afterwards the experiments exploring the influence of pressure and dopant on the V-pit density, to explore the effectiveness of pentane as dopant in reducing the V-pit density, are discussed. The methods of these experiments are explained before presenting the outcome of the experiments.

Chapter 4 begins with a description of the measurements carried out to study the pit morphology, in order to try and understand the influence of dopant and pressure on the formation mechanism of V-pits. Firstly the pit diameter is discussed, after which the orientation of the pits are considered. From this orientation follows naturally the determination of the facet angle. The last characteristic treated is the depth of the pit, before giving an overview of all characteristics in the last paragraph.

Chapter 3 and 4 are mainly concerned with the results of V-pit formation. In chapter 5 the origins of a V-pit are treated by discussing transmission electron microscopy (TEM) measurements, carried out by an external research group.

The significance of the results of the experiments treated in chapters 3 to 5 are discussed in the discussion in chapter 6. This allows to propose a model describing the formation and closure of V-pits. In the conclusion in chapter 7 the overall result of this work is presented, after which the recommendations mentioned throughout this work are summarized in chapter 8.

In the discussion some points need further elaboration, which is presented in appendix A, about curvature and stress. Appendix B covers proofs for selected formulas used in this work.

Chapter 2

Fundamental aspects

In this section fundamental aspects are covered in order to create a basic understanding of the principles governing the phenomena and apparatuses mentioned in this work.

2.1 High electron mobility transistor

The structures studied in this work are high electron mobility transistors. Their application and the physics governing their operation are discussed in this section.

2.1.1 Application

A high electron mobility transistor (HEMT) is, quite self-explanatory, a transistor with a channel with relatively high electron mobility. As other transistors it can be used in switching applications (the heart of the computing industry), for signal amplification or for power conversion. Originally HEMTs were developed for high speed applications, but after the first devices were fabricated, scientists found they exhibited a very low noise figure. Because of this noise performance they are widely used in low noise, small signal amplifiers, power amplifiers, oscillators and mixers operating at frequencies up to 60 GHz, potentially up to 100 GHz. HEMTs are therefore frequently used in radio frequency applications, including cellular telecommunications, radar, radio astronomy, or basically any application that requires a combination of very high frequency performance and low noise [3].

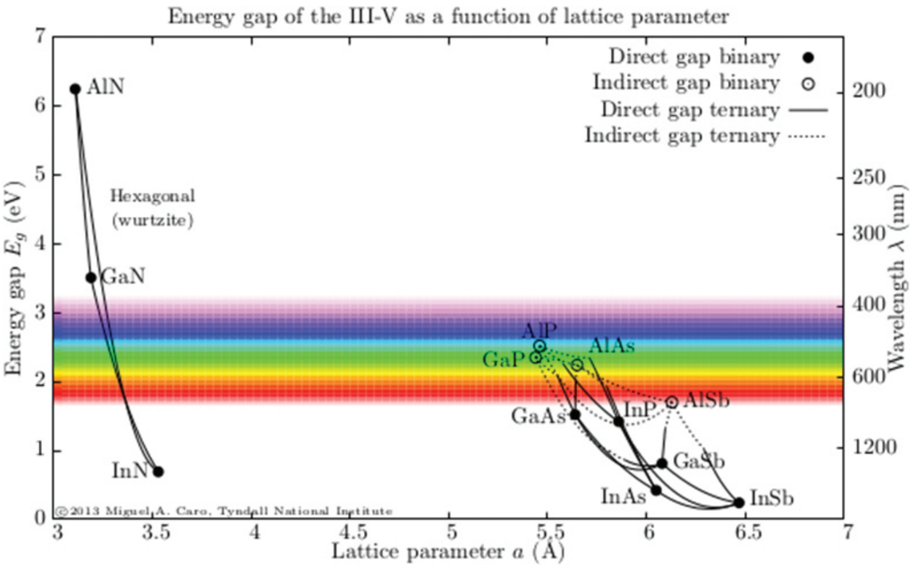

FIGURE 2.1: Band gap vs. lattice parameter for typical III-V materials. Reprinted from [6]

The actual application of a HEMT depends heavily on the materials used. Whereas HEMTs made of gallium arsenide (GaAs) can be found in cellphones and radar systems, the gallium nitride (GaN) HEMT is mainly used for high power applications, such as mobile base stations (3G and 4G transmitters) [2], power transmission lines and radio frequency power transistors [4]. This difference in application is a result of the larger band gap of GaN, allowing operation at higher temperatures and higher voltages. Current research on GaN HEMTs also aims towards applications in energy saving, exploiting the low on-resistance of the GAN HEMT compared to conventional Si-transistors [1].

2.1.2 III-N material properties

III-V semiconductors, consisting of metals out of group III and group V of the periodic table, are very common in a broad range of applications. III-N semiconductors are less common, but have been attracting a lot of attention because of their different crystal structure. In fact the Nobel prize in physics of 2014 was awarded to Akasaki, Amano and Nakamura for the invention of a LED based on III-N semiconductors, GaN specifically [5]. In figure 2.1 the lattice parameter and band gap of GaN are shown with respect to other common III-V semiconductors.

In order to build a HEMT one needs a buffer structure and a barrier layer, as will be explained in more detail later on. The ternary alloys $Al_xGa_{(1-x)}N$ (from now on just

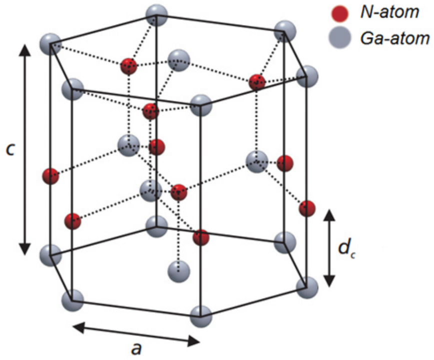

FIGURE 2.2: Sketch of wurtzite crystal structure of GaN. Adapted from [9]

AlGaN) are important in this buffer (assisting in the gradual change in lattice parameter from substrate to GaN) and the most common materials used as electron barrier. For ternary alloys many important parameters, such as the lattice parameter and electric constants, can be deduced using Vegards law [7]. This states that the parameters of the alloy are proportional to the concentrations of the individual semiconductors, i.e. linear interpolation:

$$a_{Al_xGa_{(1-x)}N} = x \cdot a_{AlN} + (1-x) \cdot a_{GaN} \tag{2.1}$$

Linear interpolation however cannot be applied to the band gap. In order to find the band gap depending on the relative concentration of both semiconductors a quadratic interpolation is more appropriate:

$$E_{g,Al_xGa_{(1-x)}N} = x \cdot E_{g,AlN} + (1-x) \cdot E_{g,GaN} + x(1-x)b^E \tag{2.2}$$

With b^E an empirical bowing parameter, in the case of AlGaN valued at 1.4 eV.[8]

As opposed to the other, common III-V semiconductors, which exhibit Zinc-Blende crystal structure, the crystal structure of a III-N material is the hexagonal wurtzite structure. The wurtzite structure (figure 2.2) is hexagonal close packed and has a sixfold symmetry. It can be seen as a set of two substructures (or bilayers), alternate planes of hexagonal close-packed N-atoms and Ga-atoms in which three N-atoms occupy the tetrahedral gaps of the Ga-layer and vice versa. The structure can be characterized by the in-plane lattice parameter a (3.189 Å)[10], the out-of-plane lattice parameter c (5.185 Å)[10] and the vertical distance of the two different atoms d_c (1.955 Å) [7].

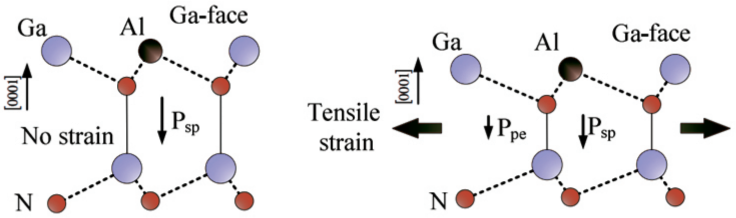

FIGURE 2.3: Polarization of AlGaN under influence of tensile strain. Adapted from [12]

2.1.3 Polarization

In a crystal lattice with two different atoms some degree of polarity (or polarization) is inherent. In completely symmetric crystals all dipoles cancel each other out, leaving zero polarization. Both AlN and GaN however exhibit a slight deviation from the ideal Wurtzite structure concerning the relative vertical distance between cation and anion. This leads to a spontaneous polarization. This asymmetry also implies that reversing the order of the bilayers gives a difference in polarity. Therefore the difference between Ga-face polar and N-face polar structures is non-trivial. For example the position of the 2DEG is different for both structures and a different height of the Schottky barrier is found [11]. It is not easy to predict the polarity of a structure, but there are numerous experiments to measure it. As it turns out almost all structures of GaN grown by metal-organic chemical vapor deposition (MOCVD) on sapphire or Si(111) substrates are Ga-face polar, so this assumption is also made for the structures used in these experiments. When the material is strained, the deviation from the ideal wurtzite structure changes. This adds an additional term to the polarization, called piezoelectric polarization (see figure 2.3). These two polarizations are crucial for filling a two-dimensional electron gas, which is a central element in a HEMT.

2.1.4 Channel formation

In a 2-dimensional electron gas (2DEG) electrons are free to move in two directions but strongly confined in the third direction. This free movement of the electrons means a 2DEG has famously low resistance. At the interface between an AlGaN layer and a GaN layer, such a 2DEG is formed in the first 1-3 nm of GaN below the interface. Looking at the band diagrams of both materials separately (figure 2.4A), one can see that the AlGaN band gap is much bigger than the band gap of the intrinsic (or undoped) GaN.

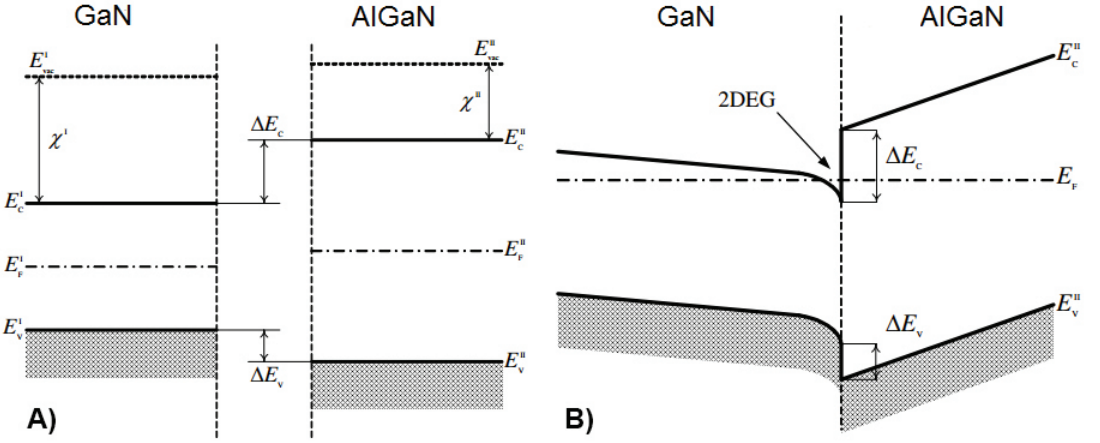

FIGURE 2.4: Band diagram of AlGaN and GaN separated A) and put in contact B). E_{vac} is the vacuum level energy, E_c and E_v the energy level of the conduction band and the valence band respectively. ΔE_c and ΔE_v indicate the difference in conduction band energy and valence band energy between GaN and AlGaN respectively. E_f indicates the Fermi level. χ is the electron affinity. Adapted from [12]

When both layers are put in contact (figure 2.4B), the Fermi levels align. This means the bands in GaN shift upwards and the bands in AlGaN shift downwards. Andersons rule [13] however states that at the interface of a hetero junction the vacuum levels should align. This results in the bands bending back to their original position. By doing so the conduction band of the GaN alligns below the Fermi level, thereby trapping electrons in a quantum well; the 2DEG. As opposed to GaAs HEMTs, that need additional doping of the AlGaAs to induce charge, the electrons filling the 2DEG are a result of the polarization.

As explained before there are two polarizations found in GaN; the spontaneous polarization built in by a deviation from the standard wurtzite crystal, and an additional piezoelectric polarization resulting from an additional displacement of the cations (Ga- or Al-atoms) and anions (N-atoms) due to strain. At the interface between the barrier and the intrinsic GaN this tensile strain is caused by a different lattice parameter and the small thickness of the barrier preventing relaxation. The spontaneous polarization in the AlGaN barrier can, similarly to the band gap, be estimated using quadratic interpolation.

$$P_{sp,Al_xGa_{(1-x)}N} = x \cdot P_{sp,AlN} + (1-x) \cdot P_{sp,GaN} + x(1-x)b^sp \qquad (2.3)$$

With b^{sp} an empirical constant, for AlGaN 0.021 C/m^2 [14]. Both polarizations work in the vertical direction and can therefore simply be added to give the total polarization.

A change in polarization gives rise to a local charge density following:

$$\rho = \nabla P \tag{2.4}$$

In epitaxy these changes in polarization occur at interfaces between different layers. When the layers are homogeneous, there is no in-plane variation. This means that there only occur jumps in charge density at these interfaces, with an according (sheet) charge density of

$$\sigma = P(top) - P(bottom) = P_{sp}(top) + P_{pe}(top) - P_{sp}(bottom) - P_{pe}(bottom) \tag{2.5}$$

In a typical HEMT structure the top layer is the AlGaN barrier and the bottom layer a thick layer of intrinsic GaN.

$$\sigma = P_{sp}(AlGaN) + P_{pe}(AlGaN) - P_{sp}(GaN) - P_{pe}(GaN) \tag{2.6}$$

The bottom layer can be considered relaxed, since it is of sufficient thickness to allow complete relaxation. Therefore the piezo-electric polarization of this bottom layer can be neglected [15]. The AlGaN layer is however always under tensile strain. The piezo-electric polarization (which now cannot be neglected) and spontaneous polarization have the same sign and add up. This leaves a positive sheet charge density, attracting electrons from the AlGaN to the interface. Put another way, the polarization in the AlGaN layer aligns itself with the positive side towards the GaN layer beneath. This creates a strong electric field (in the order of 10^6 V/cm), which drives loosely bound surface electrons and ionized covalent electrons to the interface. Here they fall into the quantum well, filling the 2DEG [16]. The spatial separation of the mobility carriers and their donors leads to an improved mobility, since the short-range ion scattering is nearly eliminated [12].

A typical HEMT is shown in figure 2.5. The source and drain contacts inject and retrieve electrons to and from the channel respectively. The gate regulates the resistance of the channel, making it possible to effectively open and shut the channel. By applying a voltage to the gate, the potential at the surface changes, giving the electrons in the 2DEG energy to escape the channel. This lowers the amount of charge carriers in the channel and therefore the current between source and drain. In other words the current

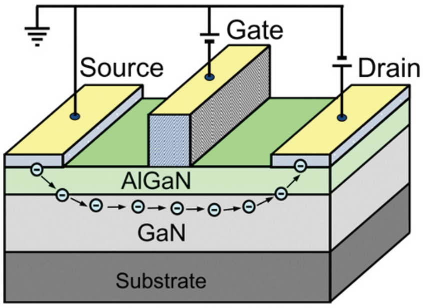

Figure 2.5: Typical HEMT device. N.B. the image is not to scale; the thickness of the layers is in reality a lot smaller than the dimensions of the contacts. Reprinted from [17]

between source and drain can be controlled by applying a voltage to the gate, the important function in switching applications of a transistor. The HEMTs fabricated at the Fraunhofer IAF are normally on transistors, meaning that the channel is open when no voltage is applied to the gate electrode.

2.2 Epitaxy

Epitaxy (from the Greek epi ($\epsilon\pi\iota$), meaning "above", and taxis ($\tau\alpha\xi\iota\varsigma$), meaning an ordered manner) is the growth of a crystalline structure one a crystalline substrate. Ideally the material being deposited forms neat layers of atoms, without distortions, building up a perfect crystal. A key element for perfect layer growth is matching of the in-plane lattice parameter. In homo-epitaxy, where the growth material is identical to the substrate material, this is logically the case. However in hetero-epitaxy, which is more interesting for applications, the growth of one material on a substrate of a different material, the lattice parameters are seldom the same. This induces strain in the deposited material, which leads to defects and therefore imperfect crystalline structure. The choice of substrate is therefore crucial in epitaxial processes. Moreover there is a multitude of methods to control epitaxial strain, a field of science that is called strain engineering. More detailed information on substrates and strain engineering is given in section 3.1.

A lot of different methods exist to grow materials, ranging from plasma enhanced pulsed laser deposition to sputtering. For growth of GaN typically two methods are used: Metal-organic chemical vapor deposition (MOCVD), also known as metal-organic vapor phase epitaxy (MOVPE), and molecular beam epitaxy (MBE). The main difference between

MOCVD and MBE is the ground materials used (organic compounds in MOCVD vs. pure metals and simple molecules in MBE) for layer growth.

In MBE an ultra high vacuum is required in order to achieve very high purity material. The materials are heated until they sublimate or evaporate. The gasses then condense on the substrate and only there they may react with other materials. When sublimated or evaporated the atoms have a very long mean free path, preventing them to react mid-air (hence the beam in molecular beam epitaxy). A large drawback of MBE is the slow deposition rate ($< \mu$m/h).

In MOCVD pyrolysis (decomposition of the gasses in the absence of oxygen) leaves the desired atoms on the substrate surface, after intermediate chemical reactions. Here they bond to the surface to form the desired layer of material. This process is significantly faster ($> \mu$m/h) than MBE, but also has higher impurity concentration (consisting mainly of carbon atoms from the organic compounds). A higher impurity concentration leads often to inferior quality of the grown crystal structure, as will be demonstrated in the main part of this work.

In this work the samples are prepared using MOCVD, mainly because of the high growth rates, which is more interesting for large scale application.

2.2.1 Metal-organic chemical vapor deposition

Chemical vapor deposition typically follows six main steps (see figure 2.6)[18]:

1. Evaporation and transport of reagents (i.e. precursors) in the bulk gas flow region into the reactor.
2. Gas phase reactions of precursors in the reaction zone to produce reactive intermediates and gaseous by-products.
3. Mass transport of reactants to the substrate surface.
4. Adsorption of the reactants on the substrate surface.
5. Surface diffusion to growth sites, nucleation and surface chemical reactions leading to film formation.

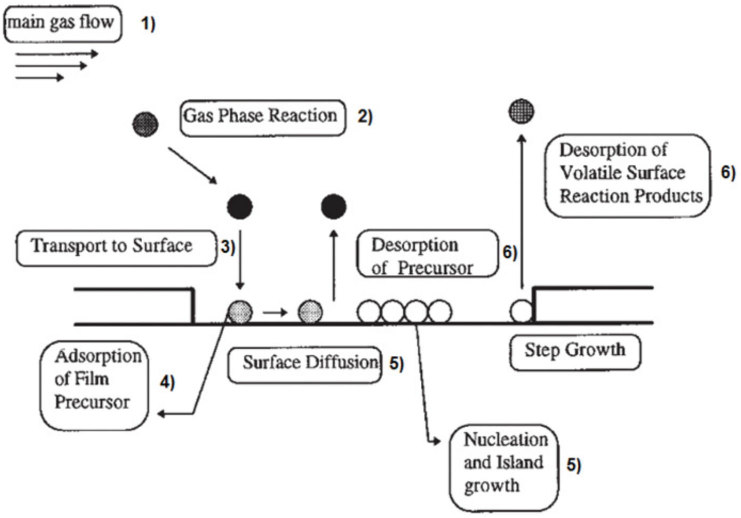

FIGURE 2.6: Typical processes during chemical vapor deposition. Reprinted from [18]

6. Desorption and mass transport of remaining fragments of the decomposition away from the reaction zone.

The growth rate typically depends on reactor pressure, substrate temperature and the III-V ratio. The substrate temperature dependence of the growth rate can be divided into three domains (see figure 2.7A). Firstly, at low temperatures (up until ca. 600°C) the growth rate is controlled by the reaction kinetics in either the gas phase or on the substrate. In this case the growth rate (GR) can be modeled using an Arrhenius equation [18]:

$$GR \sim e^{-\frac{E_a}{k_b T}} \tag{2.7}$$

with E_a the apparent activation energy of the slowest reaction, k_b the Boltzmann constant and T the temperature. Finding the proper reaction to insert in this equation is not as straight forward as one might think. The adsorption of the desired atoms at the surface is only one of many reactions at the surface[i]. In this domain high quality crystal structure is obtained by minimizing temperature variations, as the growth rate is controlled by chemical kinetics. With increasing temperature, the growth rate grows less dependent on the temperature and is mainly governed by the mass transport of the reagents to the surface (step 3). This is called the diffusion-controlled growth. At even

---

[i] To give an indication of how many different reactions there are: a typical computational study by Sengupta et al. [19] on the reactions involved, considered 52 different surface reactions (and 18 gas phase reactions).

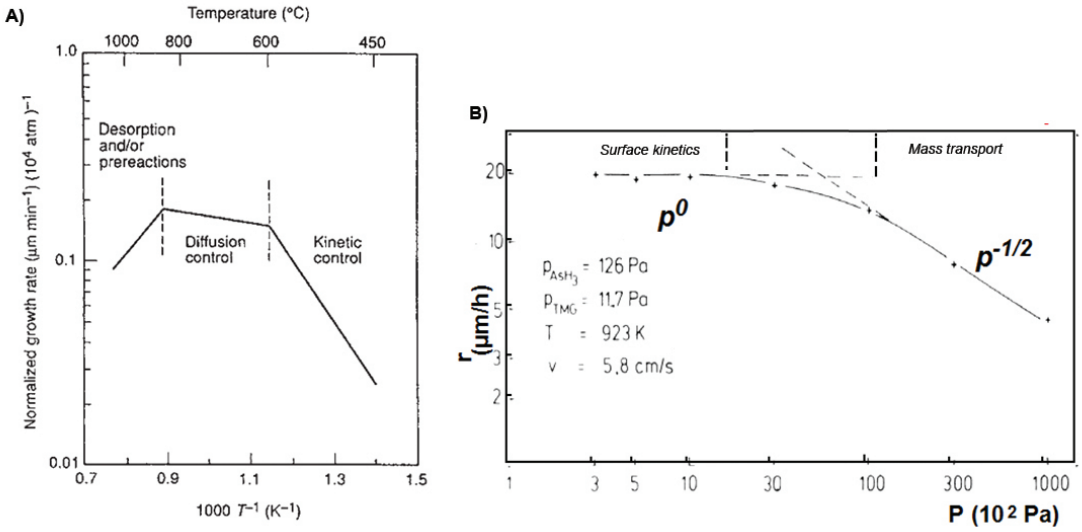

FIGURE 2.7: A) Growth rate dependence on temperature for MOCVD of GaAs. Reprinted from [18]. B) Growth rate dependence on pressure during MOCVD of GaAs. Adapted from [20]

higher temperatures the growth rate is strongly influenced by desorption of the precursors (step 6), even lowering the growth rate. The influence of pressure can be divided into two regions (see figure 2.7B). At low pressures, up until 20 mbar, the growth rate is independent of pressure and governed by reaction kinetics. At higher pressures, more than 100 mbar, the mass transport is again the prominent factor and the growth rate lowers with increasing pressure as $1/\sqrt{P}$. [20]

The III-V ratio can be influenced by changing the flow of both gasses. For increasing ammonia (the source of N-atoms) flow the growth rate of c-plane GaN is found to decrease, as for increasing trimethyl gallium (source of Ga-atoms) flow this growth rate increases [21]. This can be combined to state that with increasing III-V ratio (Ga/N) the growth rate increases.

In these experiments an Aixtron AIX2800G4 HT is used to grow the samples. This is a vertical rotating disk reactor (see figure 2.8) with eleven rotating satellites for the wafers. At point A the gasses enter the reactor via the gas inlet and flow radially outwards over the wafers (one example at B). The wafers themselves rotate to obtain homogeneous growth. Afterwards the gasses are removed through the holes in the outer ring indicated by C. The white floor and ceiling of the reactor are made of quartz and can be removed and cleaned to remove parasitic crystallized material, which eventually flakes off and contaminates the wafers during growth. The reactor is heated by a radio frequency inductor from below and furthermore equipped with thermal sensors and optical sensors

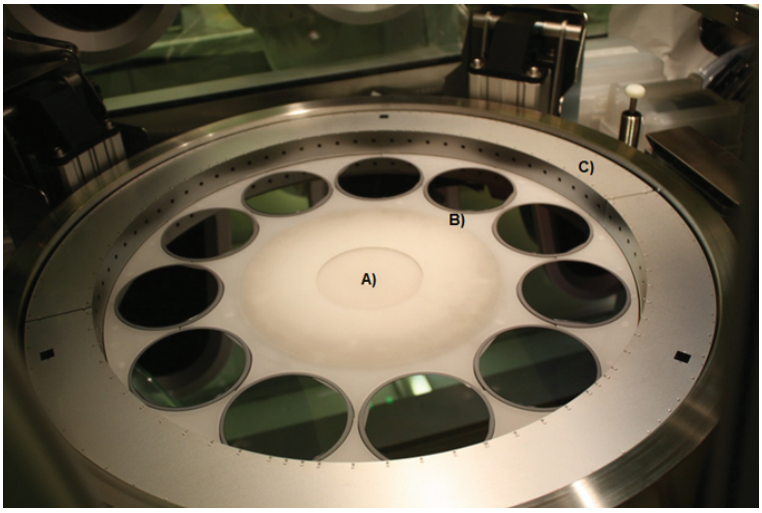

Figure 2.8: Aixtron G4 11x4″ MOCVD reactor. When the reactor is shut, the gas inlet is placed at side A) and the gasses flow radially outwards. B) individual rotating satellites containing the wafers. C) Holes through which gasses are removed from reactor.

(LayTec EpiTT) measuring growth rate and curvature of the wafers (more on this in appendix A).

The gasses are formed out of the liquid trimethyl gallium (TMG) or trimethyl aluminum (TMA) for deposition of Ga- or Al-atoms respectively, by a bubbler. Then they are transported through a series of valves, which allow control of the concentration of the gasses, by a carrier gas (hydrogen) to the reactor. Obviously there are separate lines for the ammonia and the TMG, in order to prevent them reacting before they enter the reactor.

2.2.2 Epitaxy of gallium nitride

In MOCVD growth of GaN trimethyl gallium ($Ga(CH_3)_3$) and ammonia (NH_3) are typically used as source of Ga and N respectively, as mentioned before. Trimethyl gallium starts pyrolyzing at 475°C. Therefore GaN could be grown at growth temperatures around 500°C, but this results in low quality crystal structure. High quality GaN is grown at much higher temperatures, around 1050°C. Above 1100°C the GaN starts dissociating and the grown layer starts to desorb [22]. There are two main routes for the formation of GaN to take place; the precursors reacting in the air above the surface (adduct formation) and the decomposition of the precursors at the surface (see figure 2.9). Especially the latter involves a lot of different surface reactions, making it a

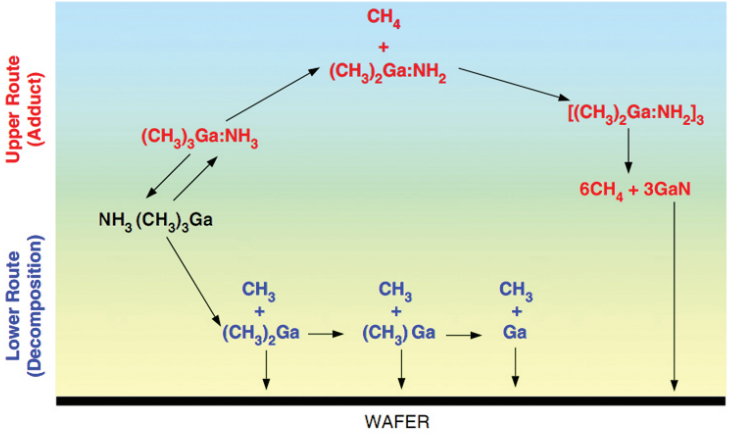

FIGURE 2.9: Reaction pathways for MOCVD of GaN. Reprinted from [23]

complex reaction scheme to study. In one computational model a preference for the surface decomposition (for a reactor similar to the one used for the growth of samples used in this work) was found [23]. More detailed information on growth of GaN (and AlN) layers is given in section 3.1.

2.3 Crystal defects

During crystal growth, atoms can get misplaced. This induces imperfections in the crystal lattice of a material that may eventually cause defects in the system. These defects can greatly influence material properties, such as its resistivity and yield strength. There are a few different types of defects, of which the ones that will be mentioned later on in this thesis will be briefly introduced.

2.3.1 Dislocations

In figure 2.10 below one can see that an atom can be misplaced in typically two ways. In figure 2.10A an atom row has placed itself in between two other atom rows, where originally there had only been sufficient space for the two atom rows. Such a line defect is called an edge dislocation. In contrast, in figure 2.10B the atom row is vertically misplaced, inducing a line defect which is called a screw dislocation. The dotted line is the dislocation line (**l**) along which the dislocation propagates. The vector **b** in the figure

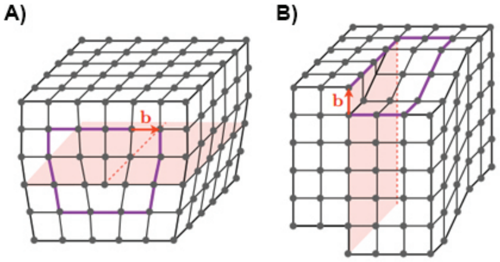

FIGURE 2.10: A) edge dislocation and B) screw dislocation. The orange vector **b** illustrates the burgers vector. The purple line is a closed circuit to find the burgers vector. The dotted line is the dislocation line along which the dislocation propagates. The orange plane describes the slip plane. Reprinted from [24].

is called the Burgers vector, proposed by the Dutch physicist Jan Burger[ii] in 1938, and describes the magnitude and direction of dislocations. This Burgers vector can be found by drawing a closed circuit around the dislocation (the purple lines in figure 2.10. In a perfect crystal, without dislocation, this circuit is indeed closed. When a dislocation is introduced there is a gap in this circuit. The vector needed to close this gap is the Burgers vector. A different way to describe the type of dislocation is looking at the angle between the dislocation line **l** and the burgers vector **b**. When **l** and **b** are perpendicular (figure 2.10A), the dislocation is of the edge-type. In case of **l** and **b** being parallel, there is a screw dislocation (figure 2.10B). When **l** and **b** are neither parallel nor perpendicular the dislocation is said to be of a mixed type. In GaN there is a significant difference in the magnitude of the burger vectors attributed to the different dislocations, since the lattice parameter for the in-plane direction (a=3.189 Å) and out-of-plane direction (c=5.185 Å) is different. Since the elastic energy of a dislocation is proportional to the square of the burgers vector, this also means that a screw dislocation has a higher elastic energy [26], an important parameter in etch pit formation (more on that in paragraph 2.4.2). Large screw dislocations are often observed in III-N materials and commonly known as nanopipes [27].

[ii] Since he was a Dutch physicist, here a short biography; Burgers lived from 1895 to 1981 and started his studies at the University of Leiden, where he came to know Albert Einstein, Niels Bohr, Hendrik Lorentz and Kamerlingh Onnes. After finishing his PhD under P.T. Ehrenfest, he moved to the Technical University of Delft where he was largely concerned with fluid dynamics, a field in which he introduced an equation which has come to be known as the Burgers equation. Alongside this work at the TU Delft he worked with his brother on crystallography, which lead to the introduction of the Burgers vector in 1938. In 1955 Burgers left Delft for the Institute of Physical Science and Technology at the University of Maryland, where he worked on the relation of the Boltzmann equation to the equations of fluid dynamics. In the summer of 1981 he died at age 86. [25]

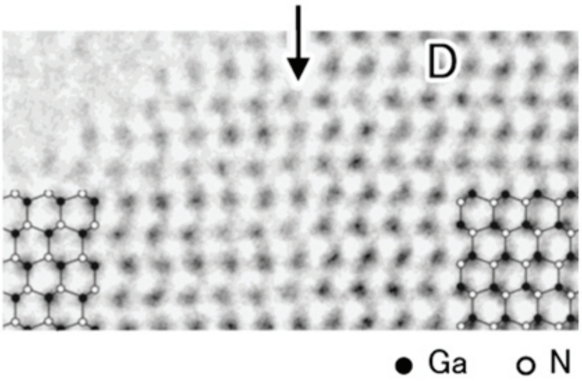

FIGURE 2.11: Inversion domain boundary (indicated by the arrow) of GaN. D denotes the domain. Reprinted from [29]

2.3.2 Inversion domain

Crystal structures containing two (or more) atoms, are usually non-symmetric with respect to exchange of the constituent atoms. For the wurtzite crystal structure this means that the occupation of the sub lattices is interchanged. When two such different formations meet each other, a grain boundary is formed. Such a boundary is called an inversion domain boundary (IDB). This is illustrated in figure 2.11. The formation energy of such an IDB is calculated [28] to be very low, only 25 meV/Å^2, depending on growth conditions this means that they will occur often.

2.4 V-pits

The appearance of V-pits, also known as inverted pyramids, is a well-known phenomenon in the epitaxy of GaN structures. Pit formation is undesirable, since they are mostly deep enough to affect the important layers (barrier and electron channel) of the HEMT structure. Typically they are known to lower the breakthrough voltage of a HEMT significantly [30]. Other research correlated an increase in pit density with a decrease in carrier mobility and carrier density [31]. For other applications, such as LEDs, the presence of V-pits is beneficial. In these systems the V-pits prevent non-radiative recombination by creating barriers to diffusion of carriers[32], increasing the light emission efficiency of the LED [33][34].

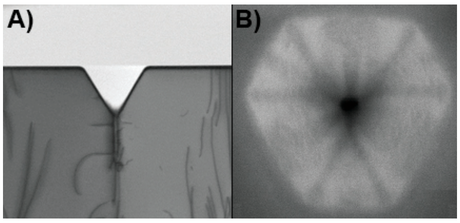

FIGURE 2.12: A) cross section and B) top view of a V-pit.

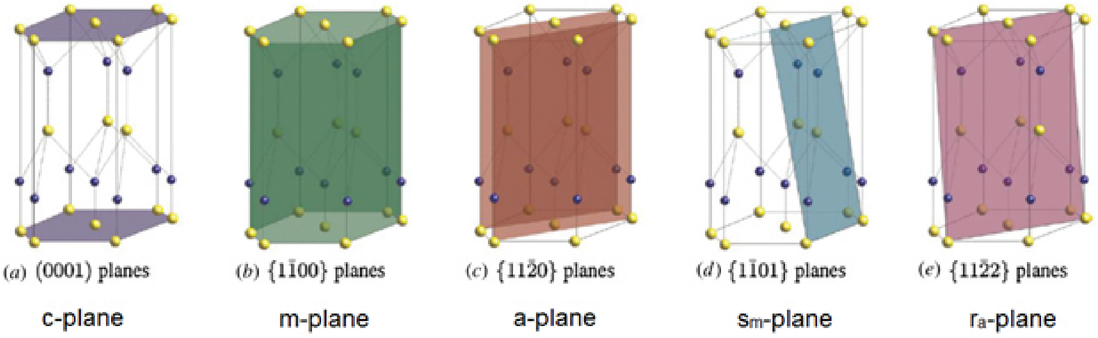

FIGURE 2.13: Different crystallographic planes in the wurtzite crystal structure. Adapted from [35]

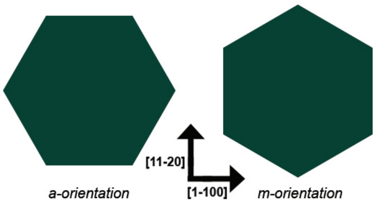

FIGURE 2.14: Possible orientations of V-pits

2.4.1 Morphology

The name V-pit originates from the cross section (figure 2.12A) of such a pit, whereas the term hexagonal refers to the six side facets such a pit exhibits (see figure 2.12B). These six side facets are a clear result of the sixfold symmetry of the wurtzite GaN. In order to be able to describe the different orientations of a V-pit, there exist a few definitions describing planes.

In figure 2.13, the most important planes are depicted. The {0001}- or c-plane (figure 2.13) is the plane as seen from the HEMT, i.e. the growth direction is along the {0001}- or c-direction. The m-plane describes the sidewalls of the basic wurtzite unit cell. The a-plane is rotated 30° (adding this to the 60° symmetry this can be seen as a rotation of 90°) with respect to the m-plane. Both a- and m-plane are perpendicular to the c-plane. Hexagonal pits can either have an m-orientation or an a-orientation, as illustrated in figure 2.14. A dodecagonal pit (a pit with 12 sides) exhibits both orientations at the same time; six sides have an a-orientation and the other six an m-orientation. While it is the established notation to refer to the tilts of the m-plane as the s-plane $\{1\bar{1}01\}$ and r-plane $\{1\bar{1}02\}$, the terminology in this work is expanded to cover similar planes in the a-orientation. A subscript is added to these tilted planes to identify which plane is tilted, an a-plane or an m-plane. This results in the following short hands: s_m-plane for $\{1\bar{1}01\}$, s_a-plane for $\{11\bar{2}1\}$, r_m-plane for $\{1\bar{1}02\}$ and r_a-plane for $\{11\bar{2}2\}$. With simple geometry one can find the angle between different lattice planes (see appendix B.1). For example for the s_m-plane the angle with the c-plane equals:

$$\alpha = tan^{-1}\left(\frac{2\,c}{\sqrt{3}\,a}\right) \tag{2.8}$$

With the (fully relaxed[iii]) lattice parameters of GaN this gives a facet angle of 62°. Measuring this value for the observed pits one can therefore identify the lattice plane of the sidewalls. This value of 62° is mostly found in literature, for both indium-containing AlGaN structures [36][37] and AlGaN HEMTs [33][38]. Only a few researches report [39][40] a facet angle of 58°, corresponding to r_a-planes, or report on dodecagonal pits [41][42].

The angle of V-pits in reality is often not precisely this theoretical value. Through adsorption, migration of atoms to the side facets and lateral growth, the bottom of the pit will fill during growth. This will decrease the apparent facet angle [40].

Different crystal orientations carry a different surface energy. Surface energy quantifies the disruption of intermolecular bonds occurring at the creation a surface. This practically means that a surface is energetically less favorable than a bulk, since there are bonds broken or not used. Indeed the surface energy is found to increase with increasing dangling bond (unused bonds) density [43]. Energy minimization strives towards diminishing surfaces with high surface energy and keeping the surfaces with low surface energy. These surface energies are extremely difficult to predict and rely heavily on the environment in which they exist. A popular method in calculating surface energies uses density functional theory. For GaN surfaces only a few of these calculations are done [44], but their applicability to this work is questionable, since the environment in the calculations is different from in the experiments in this work.

[iii] Strained lattice parameters do not affect the angle significantly.

2.4.2 Formation mechanism

Even though the V-pits are reported on regularly in literature, no complete formation mechanism exists. Literature agrees on the fact that V-pits terminate threading dislocations. There are numerous explanations for how these different threading dislocations (inversion domains [38], nanopipes [45]) are formed. A complete formation mechanism, however, linking the formation of threading dislocations to the formation of V-pits, is not yet present.

A few proposed mechanisms are describing InAl(Ga)N HEMTs, where a large role is played by segregation of indium atoms. For example Miao et al.[36] proposed that segregation of In in a InAlN HEMT around defects prevents c-plane crystal growth. This exposes the s_m planes and reduction of the strain energy is achieved by an increase in surface energy, provided by the s_m planes [46]. The indium atoms prefer these s_m planes over bulk sites, promoting growth of the pits [47]. Hiramatsu et al.[48] linked the different growth rates to different temperatures, but only considered InAlN structures, where lower temperatures are needed to incorporate indium atoms. Yang et al.[49] further validated this mechanism. Son [50], Wang [51] and Wu [52] claim reduced gallium incorporation on the side facets lowers the growth rate of the facets. Since the plane with the slowest growth rate remains[iv], this opens up the V-pit. These mechanisms unfortunately rely quite heavily on (the segregation of) indium, which is not present in the samples used in this research.

Voronenkov et al.[40] generalized the origins of a V-pit as imperfections that locally reduce growth rate. Among these imperfections are inversion domains [38][53], stacking mismatch boundaries [54], edge dislocations [39], screw dislocations [50] and mixed dislocations [39][50]. Interestingly Vennegues et al.[39] dismiss scew dislocations as possible source and attribute V-pits to edge dislocations, whereas Son et al.[50] propose the exact opposite.

Bessolov et al.[55] tried to explain the formation of V-defects through drawing a comparison with etch pits. These etch pits are also widely studied and experiments with etching give a great deal of information on defect densities of epitaxial structures. As mentioned before, pits originate at threading dislocations. By using etchants, pits are created

---

[iv] This might seem counter intuitive, but is easily explained by the fact that fast growing planes grow shut, making them disappear.

at these threading dislocations. Since these pits are much more easily observed than threading dislocations, one can deduce a pit density and translate this to a threading dislocation density. Knoke et al.[56] convincingly proved (see section 2.5.3) a correlation between the size of etch pits and the type of dislocation at the base of the pit. Weyher et al.[26] make similar observations and propose that not only the different elastic energy of the different dislocation types is source of the different sizes (Cabreras theory [57] states that the size of an etch pit is inversely proportional to the elastic energy of the dislocation), but also the inclusion of impurities such as carbon. Bessolov and his colleagues found this same parallel, but they fail to explain the part where the two formation mechanisms (one governing etch pits and one governing growth pits) overlap. Therefore its applicability to growth pits is not unquestioned.

Northrup and Neugebauer [47] propose that “the driving force for pit formation is a reduction in energy achieved by avoiding the accumulation of strained material in the region near the core of the dislocation. The reduction in strain energy is accomplished at the expense of increased surface energy, and the size and shape of the pit is affected by the surface and dislocation energetics.” They fail to explain, however, why some dislocations result in a V-pit and some do not, as found by Vennegues [39] and Son [50]. Song [58] explains that V-pits are formed in order to relieve strain at a critical thickness. Multiple other sources however discard this strain relaxation mechanism [51][59].

All in all there is no straight forward mechanism available explaining the formation of V-pits.

2.5 Inspection tools

2.5.1 Automated optical inspection

In these experiments a Rudolph Technologies NSX 320 tool for automated optical inspection (AOI) is used (see 3.2.1). This machine automatically scans wafers with a variety of microscope objectives (10x is used in these measurements) and a grayscale camera. Defects on the wafer give contrast with the proper crystal structure background. By setting a threshold value, the tool records places with high contrast (defects) found on the wafer. A 4-inch wafer can be scanned in 8 minutes. The coordinates of the defects are saved, after which a separate Mathematica routine can build up a map of defects. These defects can consist of particles, pits, cracks and in unfavorable conditions even surface roughness.

2.5.2 Scanning electron microscope

A typical scanning electron microscope (SEM) can reach magnifications in the order of 100.000x. The magnification of a microscope is fundamentally limited by the wavelength of the light, or more precisely radiation, used to image the sample (the smallest object visible has dimensions of half a wavelength). This limits the resolution of an optical microscope, using light from the visible spectrum, to around 200 nm. Using other radiation with a smaller wavelength clearly reduces the resolution and therefore increases the observed magnification. The wavelength of electrons for examples is orders lower. Electrons used in a SEM typically have energies in the keV range. Using De Broglies equation[v] relating energy (E) and wavelength (λ)

$$E = \frac{hc}{\lambda} \tag{2.9}$$

with h the Planck constant, c the speed of light. With typical energies used (5-10 keV) this gives a wavelength of 0.1-0.25 nm, increasing the resolution by roughly three orders of magnitude when compared to optical microscopes. Whereas in regular optical microscopy the magnification is controlled by the power of the objective, in SEM there is no objective and the magnification is controlled by the current through scanning coils or voltage supplied to the deflecting plates. In a SEM (see figure 2.15A) an electron beam is emitted by heating a tungsten filament cathode. These electrons are focused using one or two condenser lenses[vi] (magnetic lenses in figure 2.15A) into a spot of several nanometers. This spot scans over the surface, the beam being manipulated by the afore mentioned deflectors or coils. Each reflection is coupled to its spatial coordinate. By scanning (hence the S in SEM) the surface and putting all these reflections together in one picture the total image of the sample is built up. The resolution is than merely a matter of the size of the raster it scans (in German SEM is called Rasterelektronenmikroskop (REM),

---

[v] Actually this formula should be corrected for relativistic effects, but it suites this purpose of just comparing orders of magnitude.

[vi] Using the term lenses creates the mental image of pieces of glass, but in this case it is a set of coils wrapped around an iron core that create a magnetic field, deflecting the beam into focus.

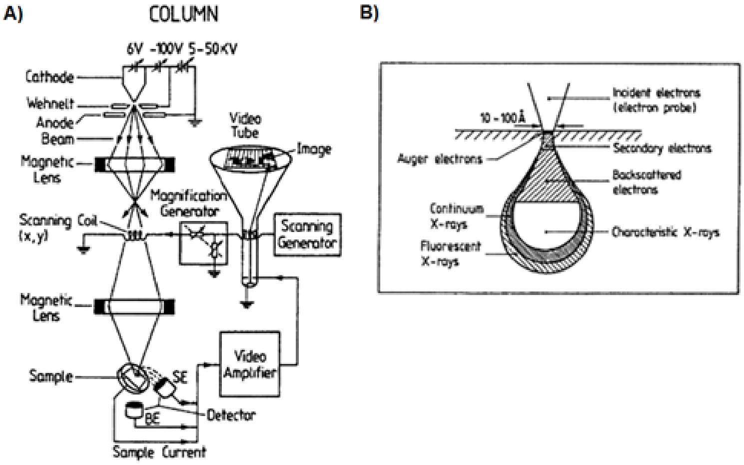

FIGURE 2.15: A) Overview of components of SEM. B) Pear shaped interaction zone of impinging electrons. Adapted from [60]

referring to the raster that is scanned); the smaller the individual images in this raster, the higher the final resolution [60].

As opposed to regular microscopy, the image recorded by a SEM is not built up merely by the reflected light, or in the case of SEM thus the reflected electrons. As can be seen in figure 2.15B below the high energy electrons are able to penetrate and interact with atoms several micrometers deep in the sample. Through inelastic and elastic scattering the electrons reach a pear shaped region in the material and several kinds of radiation are emitted. All these different kinds of radiation can be captured by different sensors. The primary source of the image is the by elastic scattering reflected primary electrons, which is very similar to regular microscopy. Another important source is emission of secondary electrons that are emitted by atoms in the material after electrons are adsorbed after inelastic scattering. These two sources are linked to two different detectors (BE and SE in figure 2.15A above). These secondary electrons are mainly used in imaging of strongly tilted samples.

In these measurements a Carl Zeiss Gemini FESEM is used, equiped with a Carl Zeiss 1540 EsB detector. The images are typically made with 5 keV electrons.

2.5.3 Transmission electron microscope

Like a SEM, a transmission electron microscope (TEM) benefits of the short wavelength of electrons to depict high resolution images of microscopic details. The main difference

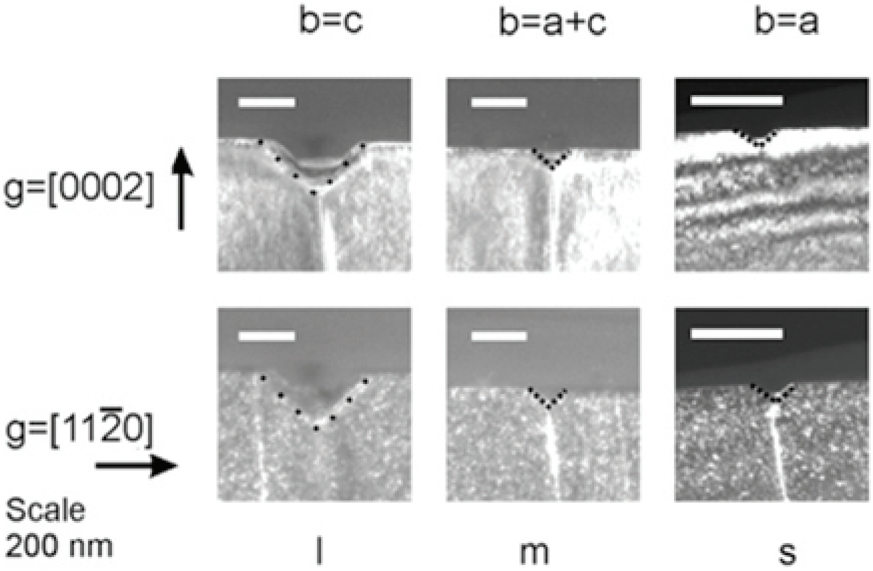

FIGURE 2.16: TEM images showing different pit sizes (large, medium and small) for two different reflections. g indicates the two different reflections to image the sample. b represents the Burgers vector with c indicating a screw dislocation, a an edge dislocation and a+c a mixed dislocation. Reprinted from [56]

.

between these electron microscopes is the electrons used to build up the image. Where SEM uses backscattered and/or secondary electrons, at TEM the detectors pick up electrons transmitted (and elastically scattered) through the sample. A relatively young technique, scanning transmission electron microscopy (STEM) combines the scanning property of the SEM and the very high energy electrons of TEM to obtain even higher resolutions. The use of transmitted electrons immediately sets an important constraint of TEM: the samples have to be very thin, under 500 nm to study defects and under 100 nm for atomic resolution. If the sample is thicker, too many electrons get absorbed in the sample and too few get transmitted to illuminate the photo sensors. This makes the sample preparation and important part of TEM measurements.

TEM is also a suitable method to study dislocations through the invisibility criterion. This criterion states that a dislocation with a Burgers vector non-parallel to the strong reflection $\boldsymbol{g_1}$ is invisible for that reflection (a reflection indicates the crystallographic direction under which the electrons hit the sample). The Burgers vector can be deduced if the dislocation is invisible for a second reflection $\boldsymbol{g_2}$, which itself is orthogonal to reflection $\boldsymbol{g_1}$, than it is orthogonal to both $\boldsymbol{g_1}$ and $\boldsymbol{g_2}$; $\mathbf{b} = \boldsymbol{g_1} \text{ x } \boldsymbol{g_2}$. This allows to differentiate between edge and screw dislocations, as for example demonstrated by Knoke et al.[56]. In their research they found a correlation between the size of V-pits and the type of dislocation they were terminating. This is elegantly demonstrated in figure 2.16. Using two orthogonal reflections they found that for large pits the dislocations disappeared at one reflection, and for small pits at the other. For medium pits the dislocations show up for both reflections. This suggests firstly that the dislocations at pits of different sizes are not the same. Since the horizontal plane of the hexagonal lattice is largely symmetric, there are only the vertical and the horizontal burgers vector. This enabled Knoke and his colleagues to attribute the screw dislocation to the large pits, edge to the small and mixed to the medium pits respectively.

Chapter 3

Pit reduction

In this chapter some more theory on epitaxy of GaN and AlGaN is discussed, in section 3.1, using the typical structure of the samples as a guide. Then in 3.2. the measurements concerning pit density are presented, along with the first results.

3.1 Sample structure

In this research three different species of samples are compared. All samples are MOCVD grown epitaxial structures for HEMT application. The buffer structures untill the first (doped) GaN layer (GaN:C in figure 3.1) are for all samples the same. The choice of buffer structure followed from years of experience in epitaxy of GaN on Si and sapphire at the Fraunhofer IAF. The difference between the samples is discussed later on in section 3.1.6.

3.1.1 Substrate

The choice of substrate is of great importance in epitaxy, as earlier mentioned in chapter 1. One ideally has a substrate with a lattice parameter and a thermal expansion coefficient close to that of the growth material. When there is no possible candidate to suit

---

[i] To offer a mental image of the relative size of the different layers; the important layers for the transistor (the [2DEG at the bottom of the] barrier) only measure some 30 nm in thickness, compared to a buffer of some 4 μm. That is to say if this report represents the important two layers, with some 1.5 cm in thickness, it would be separated from the floor by a buffer/stack of books 2 meters high (which coincidentally more or less represents all the books and papers I read as a student). If you would include the substrate, 675 μm thick, in this comparison, it would be as big as the Eiffel tower.

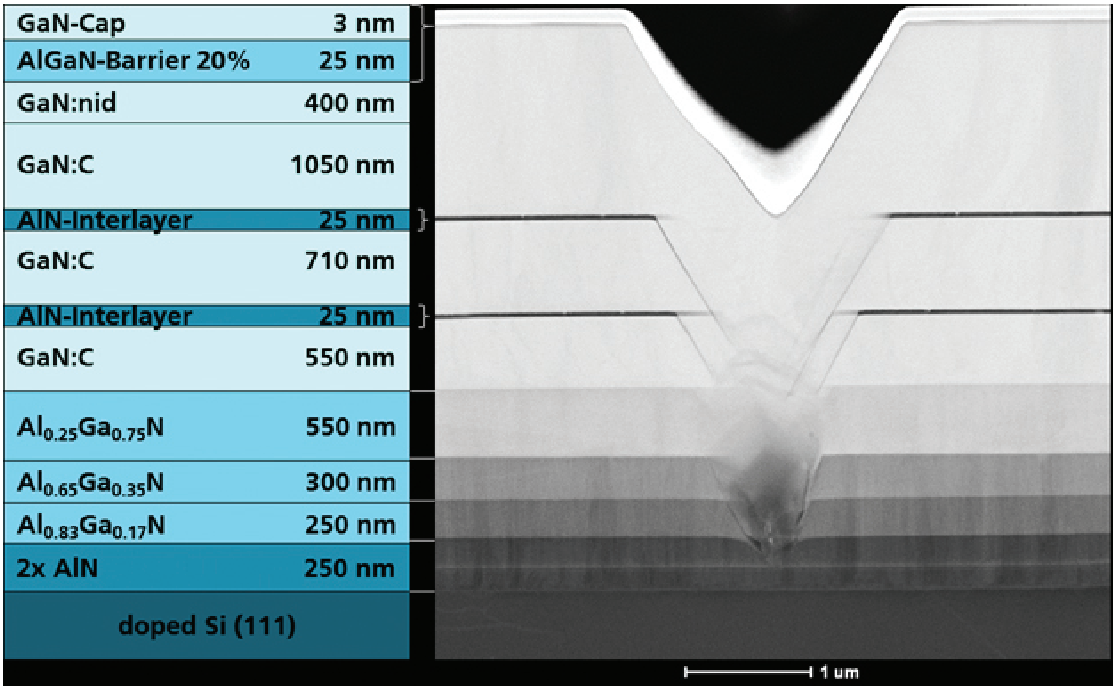

FIGURE 3.1: Schematic buffer structure and high-angle annular dark-field STEM image of the typical HEMT structure used in these experiments. N.B. The relative size of the layers in the left part 2.1 is not to scale[i]. The white layer on top of the structure is a contrast material applied at the preparation of the sample for the TEM measurement, and is thus not part of the HEMT structure itself.

these both requirements, a proper lattice parameter is preferred over a suitable thermal expansion coefficient. A large lattice mismatch is namely harder to compensate for than a large difference in expansion upon cool down. These are not the only two important parameters however. For example sapphire (Al_2O_3) is a relatively often used substrate[ii]. It has a relatively large lattice mismatch of 13% [61] and additionally a very poor heat conductivity. This makes for low heat dissipation, creating difficulties with cracking [62] and decrease of electron mobility [63]. Silicon Carbide (SiC) is another suitable candidate, with a wurtzite crystal structure, and therefore matching lattice symmetry, and a lattice mismatch of only 3%.[61] SiC substrates are very expensive however, making them unsuitable for fabrication on a large scale.

Naturally there is a great interest in common and cheap substrates. Si(001) would be a highly suitable substrate in terms of cost effectiveness and applicability, as it is the substrate most commonly used in the silicon industry. Unfortunately the fourfold symmetry of Si(001) allows for multiple preferred orientations of the sixfold symmetric

---

[ii] Sapphire was popular in the time of pioneering of epitaxial GaN and simply because there is a lot of experience in using this as substrate it remains a popular choice, even though it has a large lattice mismatch.

AlN, leading to polycrystalline layers. Polycrystalline layers are inherently linked with grain boundaries and therefore high surface roughness and defect densities [64]. Si(111) does exhibit a sixfold symmetry, just like GaN and AlN, which lowers the amount of grain boundaries (they are still present since there are still two different orientations[iii] possible). Moreover the most common reconstruction of Si in the presence of hydrogen (as mentioned before the driving gas in MOCVD and thus ubiquitously present) is a (1x1) reconstruction [64]. This means the sixfold symmetry remains intact. The large drawback however is a large lattice mismatch (17%), and a large difference in thermal expansion coefficient (50%) [65]. The fact that Si(111) is used in spite of the unsuitable parameters is a good example of the preference of industry for low costs over high quality.

A famously expensive substrate is diamond. Its thermal conductivity is a factor 4 larger than SiC [66]. Instead of growing GaN on diamond, the diamond is grown (also by chemical vapour deposition) on the GaN. In order to do so, the GaN is firstly grown on a Si-substrate, after which the structure is flipped and mounted onto temporary carrier. The Si-substrate is etched away and diamond is grown in its place instead. The temporary carrier is then removed, leaving a GaN epitaxy structure on diamond [66]. The diamond substrate is therefore purely aimed at application purposes and not suitable to grow GaN on.

In these experiments 675 μm thick Si(111) substrates from Si-mat are used. The 100 mm substrates are negatively doped with arsene, which lowers the resistivity to 0.001-0.005 Ωcm. A high resistive substrate is more favorable, since it increases breakthrough voltage, but such a silicon substrate tends to crack or even break at the high growth temperatures of GaN due to a different internal tension.

3.1.2 Seeding layer

For almost all structures concerning GaN on Si substrates, the first layer grown on the Si substrate is a seeding layer of AlN [67]. This is done to avoid contact between gallium and the silicon substrate. When they do come in contact, they react heavily to form gallium-silicon-nitrogen alloys. These reactions, known as meltback etching reactions, create holes in the substrate, which is clearly bad for the epitaxial structure build on top of the substrate, since it disrupts ordered growth. AlN is chosen as material for

---

[iii] The two orientations are a- and m-orientation, as explained in section 2.4.1

the seeding layer as it exhibits the same sixfold symmetry as GaN and moreover has a very similar lattice parameter to that of GaN (3.19 Å for GaN against 3.11 Å for AlN [7]). This makes it relatively easy to grow GaN on the AlN layer afterwards without much strain. The lattice mismatch between AlN and Si(111) (3.84 Å) however is a great source of strain and therefore threading dislocations.

High quality AlN is grown at high temperatures (above 1100°C). It turns out, however, that GaN grown at these temperatures showed a high dislocation density due to inclination of the c-axis and inversion domain boundaries [68]. At lower temperatures (around 1050°C) the GaN was of a significantly higher quality. At much lower growth temperatures for AlN (around 630°C) the quality appeared even higher [68]. Common practice is to firstly grow a low temperature (LT) AlN layer on the Si-substrate and then a high temperature (HT) AlN layer on top of this LT layer. The total AlN seeding layer should be thicker as 100 nm to form an adequate diffusion barrier for the gallium atoms [69].

In these experiments the different structures are grown on so called templates, Si-substrates with an AlN seeding layer grown on top of them. These templates are grown in reactors with clean quartz ceiling and bottom parts to prevent gallium desorbing from them and inducing the meltback etching. Fabrication of templates is done as follows: the substrates undergo a desorption step at 1200°C during 15 minutes to get rid of any adsorbents, before growing a LT (1080°C) AlN layer during 5 minutes. Afterwards the temperature is ramped to 1280°C in order to grow a final HT AlN layer for 20 minutes. The templates are then cooled to room temperature to conclude the fabrication of the templates. Growth of the HEMT structure later on begins with a similar procedure for the growth of an AlN seeding layer. This creates an AlN seeding layer of 250 nm thickness in total. The bright line that can be seen in this seeding layer in figure 3.1, is the interface between the AlN layer of the template and the seeding layer grown at the start of the HEMT growth.

3.1.3 Buffer layer

A difference in lattice parameter and thermal expansion coefficient between the substrate and the grown material causes strain, as mentioned earlier in chapter 2. A large difference in thermal expansion coefficient, combined with high growth temperatures, is a great source of tensile strain, especially during the large drop in temperature during cool down after the growth is completed. In order to avoid crack formation, one can apply different strategies of controlling this strain upon cool down. The main aim of strain engineering is to build in compressive strain to compensate the tensile strain resulting from cool down at the end.

A first method in strain engineering is a graded buffer. Several layers of AlGaN with diminishing Al content are grown on top of the AlN seeding layer. This can be done gradually, resulting in a continuous gradient from AlN to GaN [69][70], or in steps [71][72]. There are several parameters that can be changed, such as the Al content in the steps, the amount of steps and the overall thickness of the buffer. If the material quality, especially of the AlN seeding layer, is high, this can induce a compressive stress on the GaN layer grown afterwards [73]. Leung et al. [71] observed through TEM measurements, that the dislocation density decreases for each subsequent AlGaN layer. They attribute this to the dislocations bending and annihilating each other near the surface of each AlGaN layer.

A second method is the use of multilayers, also known as superlattices. The single AlN seeding layer on the substrate is usually of too low quality to induce compression. A thin layer of GaN grown on this seeding layer would grow fully relaxed, so no compressive strain is built in. This would result in cracking at cool down, since there is no force counteracting the tensile stress. The GaN is of significantly higher quality however than the seeding layer. Growing an AlN layer on top of this thin layer of GaN causes the AlN to grow fully strained or partially relaxed. The following GaN layer grown on top of this AlN layer adapts the lattice parameter of the AlN layer, making it grow compressively strained. By repeating this process (typically 50-100 times) a significant compressive strain can be built in [74], to eventually counteract the tensile strain at cool down [73].

The last method makes use of AlN interlayers [75]. The introduction of thin layers of AlN has a similar effect as the multilayer described above; the AlN is grown strained on a thick GaN layer, after which the subsequent GaN grows compressively strained on the AlN interlayer. The thickness of the interlayer is a measure of the compressive strain introduced to the system, since the AlN can relax. The difference in lattice parameter between relaxed AlN and GaN is bigger than between partly strained AlN and GaN, and therefore the compressive strain of the GaN layer above the interlayer. However fully relaxed AlN can also cause crack formation in the GaN layer beneath the interlayer [73].

In the structures used in this research the samples are grown with both a step-graded buffer and two interlayers. The step-graded buffer consists of three steps; firstly a 250 nm thick layer with 83% Al content, then a 300 nm thick layer of 65% Al and lastly layer of 25% Al, 550 nm in thickness. The actual amount of Al can be measured after the growth with X-ray diffraction (XRD) measurements. The measured content was between 80.6 and 81.6% for the first layer, 63.3-64.2% for the second layer and 21.8-23.4% for the third layer. The interlayers consisted of 25 nm pure AlN. These layers were too thin to measure their actual Al-content with XRD.

The choice for this structure follows from years of experience with growing GaN on Si(111) at the Fraunhofer IAF.

3.1.4 Carbon doping

As explained before, HEMTs made from GaN are mainly used in high power, high voltage applications. This means that the buffer layer, all layers between the 2DEG and the substrate, should have a high resistance to avoid a breakthrough of a leakage current to the substrate. A significant leakage current (commonly a leakage current three orders lower than the devices maximal output current is considered significant) reduces the switching efficiency of a HEMT. [12] The breakthrough voltage therefore is an important characteristic of a GaN HEMT. In order to achieve this high resistance the GaN layers can be doped.

Popular dopants to increase resistance are iron (Fe) and carbon (C), of which the latter is the most popular. When carbon is introduced into the GaN it can take one of two possible positions; a Ga-vacancy (cation) or an N-vacancy (anion). Carbon on other, interstitial sites has a high formation energy, and is therefore unlikely to exist in great numbers [76]. Depending on which place the carbon occupies, it acts as a donor (Ga-vacancy) or an acceptor (N-vacancy). It is found that the carbon introduces deep acceptor-like trap states [77][78], implying that the carbon predominately occupies N-vacancies. Trap states are vacancies within the band gap of a semiconductor [79]. Acceptor-like states, also known as electron traps, are electrically neutral when empty and become negatively charged when they capture an electron. Shallow states lie close to the conduction band (of AlGaN) and have low ionization energies, in the order of thermal energies (k_bT). Carbon at an N-vacancy has a high ionization energy of around 0.9 eV [78] and is therefore considered a deep trap, further away from the conduction band.

These deep electron traps compensate conduction promoting impurities such as oxygen and silicon, thereby increasing the potential barrier at sub-grain boundaries [80]. Since the conductivity of GaN is controlled by these potential barriers through the so called grain boundary controlled transport model [81][82] a high concentration of carbon decreases the conductivity of the GaN layers. Indeed the breakdown voltage increases linearly with the trap density [83], therefore a higher carbon concentration increases the breakdown voltage.

Apart from increasing the breakdown voltage, the carbon concentration also influences the characteristics of the 2DEG. A high carbon concentration near the 2DEG is found to decrease the carrier mobility and density of the HEMT [84]. Also the acceptor-like traps formed by the carbon atoms are said to induce current collapse [85]. This is an effect that increases the ON-resistance of the HEMT during high voltage application of the device and degradation of the drain current [17]. A detailed mechanism that describes current collapse is however still not available.

Carbon is already present in GaN layers, even without the intention of doping the layer. The most likely source of these carbon impurities is hydrocarbon left at the surface after decomposition of the precursor TMG [86]. Another possible source is the little CO or CO_2 that can be found in NH_2 [iv]. As explained before, the carbon tends to occupy N-vacancies. This is caused by the high flow of hydrogen preventing the NH_3 from dissociating, creating N-vacancies with low energy formation for carbon to occupy [88]. The concentration of carbon is found to decrease with increasing pressure and temperature. With increasing TMG flow rate the concentration only increases slightly, suggesting that there are mechanisms at work that remove carbon from the surface or suppress its incorporation in the bulk [89]. Investigation of these parameters at the Fraunhofer IAF by Stefan Müller agrees with the correlations for temperature and pressure. In contrast with the findings of Koleske et al. [89] the carbon concentration

---

[iv] The CO and CO_2 are byproducts of the reforming reactions used to generate H_2 from CH_4 in the synthesis of CH_3 [87]

increases more strongly with increasing TMG flow. An increase in NH_3-flow lowers the carbon concentration. Both these correlations concerning flow of precursors imply a surplus of Ga-atoms and a deficit of N-atoms, supporting the mechanism of carbon occupying N-vacancies.

In the samples used, there are two different ways of doping the GaN with carbon; adjusting growth parameters (following the earlier mentioned correlations) to include higher concentrations of carbon from the Ga precursor, and introducing a different gas (pentane) exclusively for doping purposes. Unfortunately there is no literature available on using pentane as dopant. Therefore there are no known correlations between the growth parameters and carbon concentration for the growth using pentane. Due to the complicated reaction schemes of MOCVD growth it is not possible to find a simple comparison for the carbon incorporation.

The third species of samples is grown at high temperature to reduce V-pit density. Without the addition of pentane, this induces a lower incorporation of carbon. All species have such an n.i.d. GaN layer directly beneath the 2DEG. This is done to avoid the earlier mentioned decrease of carrier mobility and density of the 2DEG by a high carbon concentration.

3.1.5 Barrier and cap

The function and physics behind the AlGaN barrier have already been treated in chapter 2. The Al-content of this barrier is typically 20-25%. Higher contents can be beneficial due to higher breakdown voltages, but the growth of AlGaN-layers with high Al content is still a big challenge and it is found to be difficult to attach low resistance ohmic contacts to this high Al content AlGaN [59]. Other research pointed out that a thin barrier gives more stable devices [90][91]. This correlation is attributed to the lower strain in thinner barrier layers. Since an operational HEMT experiences additional electrical strain (the reverse effect of piezoelectricity), counteracting the initial strain, the initial strain due to a thin barrier is additionally designed to prevent cracking over time. In this research a barrier of 25 nm and 20% Al-content (19.8-21.2% from XRD measurements) is used. This is thicker than reported in literature [90][91] and therefore induces a higher strain, but the lower Al-content (compared to examples from literature) decreases the strain.

The final layer, topping off the HEMT, is a thin layer of GaN. Although it is only several nm thick, it can have a significant effect on the HEMT performance. The cap shields the barrier from high electric fields applied by the gate. This reduces the electric strain (caused by inverse piezoelectric effect) and therefore crack formation [92][93].

In these experiments a cap of approximately 3 nm is used. Applying a consistent cap thickness between different runs is difficult due to sublimation of the cap at the high temperatures after finishing its growth. Therefore a thicker layer is grown, anticipating the reduction in thickness by this sublimation. The resulting thickness might differ between the different samples. The thickness is not measured, since this is very difficult for such a small layer with low contrast with AlGaN. In light of these experiments the cap is of very low significance, since the pit size is of two or three orders of magnitude bigger than the cap thickness.

3.1.6 Sample selection

As mentioned before there are three species of HEMT structures used in this research. In table 3.1 the growth parameters are given for the different runs of these species. The nickname is used in graphs and throughout the text. From this table it will be clarified how the influence of different parameters can be explored.

Run M0830 and M0860 are grown with the same pressure and temperature, but with a different dopant. This allows investigation of the effect of carbon doping. Run M0825 and M0860 have a similar carbon concentration and the same reactor temperature, but a different pressure. Comparing these two runs gives information on the effect of pressure. The dopant in both runs is different however, so any differences between the runs cannot be attributed to a pressure difference solely, there might be an influence of the dopant. Furthermore the surface temperature of run M0825 is significantly lower than at run M0860 as a result of the lower pressure[v]. This effect should also be included when attributing any phenomena to a pressure difference.

Another important difference between the samples is their maturity. The low pressure samples (run M0825) are made using a recipe that is improved over a long time, whereas the high pressure samples are made with relatively young, not optimized recipes. The

---

[v] This is not a setting controlled externally, but a result of the higher pressure resulting in more cool gasses near the surface, lowering the surface temperature.

Table 3.1: Growth parameters for the different sample runs used in these experiments. With [C] the carbon concentration, P the reactor pressure, T_r the reactor temperature and T_s the surface temperature.

Run number (wafer number)	**Nickname**	**Dopant**	**[C]** (cm^{-3})	**P** (mbar)	$\mathbf{T}_r$ (°C)	$\mathbf{T}_s$ (°C)
M0825 (7,11)	A2, A1	precursor	$7 \cdot 10^{19}$	36	1090	945
M0830 (2)	R1	n.i.d.	$2 \cdot 10^{17}$[a]	200	1090	1015
M1007 (6)	R2	n.i.d.	-[b]	200	1090	1015
M0860 (4,11)	B1, B2	pentane	$9 \cdot 10^{19}$	200	1075[c]	1015

[a] Lower detection limit (of secondary ion mass spectroscope).

[b] No data available, but assumed similar to the other n.i.d. sample.

[c] The set temperature was 15°C lower, since the reactor had a new ceiling. These new ceilings reflect more, since there is less buildup of crystallized material from previous runs on it. This increases the temperature at the wafers. This increased temperature is measured for the graded buffer layers, but disappears for the (doped) GaN growth.

epitaxy of GaN on Si is immensely complex and develops mostly through experience, simply because there are too many parameters to explore their effect individually. The pentane doped samples which are used, originate from a very early stage of development, and thus might not be of optimal quality. In conclusion there are three different samples, allowing investigation of the influence of type of dopant and the influence of pressure (and temperature combined).

3.2 Defect density

To measure the influence of the earlier mentioned growth parameters on the defect density, several methods are available. These are discussed in section 3.2.1. In 3.2.2 the results are presented and their significance discussed.

3.2.1 Method

Goal of this research is to study the influence of growth parameters, specifically the type of carbon dopant, on the density of V-pits. In order to achieve this several methods could be used; an optical microscopic, an AOI and a SEM. The three different methods have their specific pros and cons, which are presented in table 3.2 below.

The first option, using an optical microscope manually, is clearly the least attractive option. The optical magnification is sufficient to study pit density, but the process

Table 3.2: Properties of different inspection methods considered for these experiments.

Method	**Inspection rate**	**Inspection area**	**Inspection detail**	**Reproducibility**
(Manual) optical microscope	Medium	3 x 100 mm^2	Medium	Bad
Automated optical inspection (AOI)	Fast (entire wafer in 8 min)	Entire wafer	Low	Good
Scanning electron microscope (SEM)	Slow (1 mm^2 in 30 min)	3 x 1 mm^2	High	Good

is not very fast. Above all the reproducibility is very bad, since there is no practical way to insert the sample consistently. Little rotations are easily made, making it very hard to find the same spot on the wafer in two different measurements. Moreover the magnification is not sufficient to study the pit morphology in detail. Additionally the optical microscope does not allow tilting of the sample, an important functionality as will be explained in section 4.3.1.

The second option, the AOI, can scan the entire wafer very quickly, an entire wafer in 8 minutes. As explained before in paragraph 2.5.1, AOI does not specifically record pits, but just anything that has contrast with the background (see figure 3.2A below). In some wafers this could be just some surface roughness, creating contrast, particles that have dropped down from the reactor ceiling, or cracks. Normally the Mathematica routine filters out the cracks , but as can be seen in figure 3.2B this is not always the case. These cracks are seen by AOI as a large number of defects, a number much larger (typically one or two orders of magnitude larger) than the number of pits surrounding the crack. This gives a highly distorted defect density, which is calculated with a simple Mathematica routine (figure 3.2C). For this reason AOI scores low on inspection detail. The error margin in the measured defect density is typically 10%. A different method is needed in order to change the AOI measurements on defect density, in a (for this research) more interesting pit density.

This different method is the third method; the SEM. Due to its extremely high magnification the detail level is very high. The large drawback is the slow operation process. Loading samples takes long and the high magnification makes the area possible to inspect very small. Locating the small area therefore takes a significant amount of time as well. One clearly cannot measure the entire wafer using the SEM, so specific sections

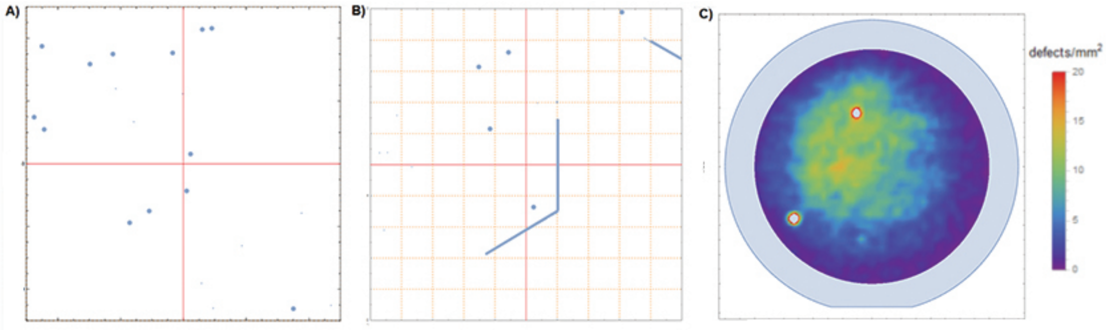

FIGURE 3.2: A typical defect map (1x1 mm) made using coordinates recorded by AOI and a Mathematica routine. B) Cracks recorded by AOI (10x10 mm). C) Defect density color map (100x100 mm). N.B. the two high density regions are not the high density regions measured as mentioned in the text, since they are clearly not representative for the entire region.

are chosen for closer examination. The results of these specific measurements are then extrapolated for the entire wafer.

Since the density of defects is quite low (in the order of 1 mm^{-2})[vi], one cannot simply scan the surface and find pits by pure luck . Fortunately the defect density measurement done by AOI saves the location of defects, building up a defect map, which can be used to simplify the search for pits. One important difference between AOI and SEM however is the consistency in which the wafer enters the apparatus. In AOI this is done automatically (by an intricate automatic edge finding and wafer positioning routine), whereas in SEM one has to insert the wafer manually. This introduces an inconsistency in the coordinate system used in both apparatuses; one cannot instantly use the map of AOI without adjusting the coordinate system of the SEM.

To align both coordinate systems one has to find the corners of the flat (a wafer is not completely round, but has one flattened side to have a clear reference point) of the wafer, which actually is what AOI does automatically. Aligning the flat horizontally, i.e. rotating the sample until both corners have the same y-coordinate, the rotation misalignment is overcome. To additionally adjust for the difference between AOI and SEM in definition of the origin of the coordinate system, one can find the middle of the wafer by applying Pythagoras theorem (see figure 3.3A). By measuring the x-coordinates of the corners of the flat one can find the distance x_c (half the difference between the

---

[vi] At 1/mm^2 defects, finding a pit by luck is like trying to find a DVD laying on the ground on de Dam in Amsterdam or the Alexanderplatz in Berlin. Sure, it is possible (if it does not get stolen before you find it), but it would be much easier if there is a way to reduce the problem to finding a DVD in your own backyard. It would save a lot of traveling as well.

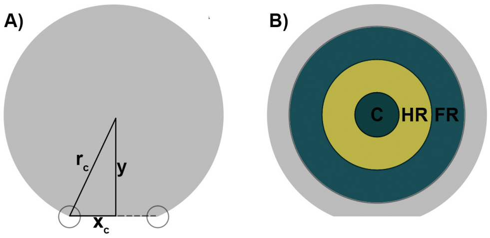

FIGURE 3.3: A) Using Pythagoras theorem to define the coordinate system for SEM. B) Definition of the wafer regions.

x-coordinates). The radius of the wafer is known (in this research 50 mm), so the y-coordinate of the wafer middle is $y_c = \sqrt{r_w^2 - x_c^2} + y_{flat}$.

After aligning the wafer in SEM, one can start examining the defects found by AOI. In most cases the specific areas measured were high defect density areas, in order to increase the inspection rate. Furthermore these areas were categorized in three different regions (see figure 3.3B). The regions are the center of the wafer (r<10mm), at half radius (10 mm<r<25 mm) and near the full radius (25 mm<r<40 mm). Here it is specifically mentioned near the full radius, since at the full radius (40 mm<r<50 mm) the grown HEMT is highly defected for all samples. For this reason this area is not used in further development of the HEMT and therefore also not measured by AOI. The definition of the regions is made based on the distance from the center of the wafer. Considering this distance the regions appear similar in size; (10:15:15). However since the area of the region increases quadratically with increasing radius, this surface area of the regions is not quite comparable (100:525:1075). This is in most cases not a problem, but does give a different weight to the regions when taking an average over the entire wafer. One can see this effect later on in the results, where the average value lies closer to the full radius values than one might expect.

As mentioned before these entire regions are too big to measure precisely by SEM. For each region (center, half radius and full radius) one or two specific high density sections are studied. It should be noted that the high density of the section is chosen to speed up the process, i.e. increase the inspection rate, but is still of a representative density for the entire region. A map containing the positions of the defects in this section (see figure 3.2A) is used to locate the defects. The local pit density was calculated by checking how many of all the listed defects in this section were pits. This gave a correction factor (for example 9 pits out of 16 defects found gives a correction factor 9/16=0.56) which was used to convert the defect density given by AOI in a pit density. An additional correction factor was applied for wafers showing cracks in the AOI map (figure 3.2B). The number of defects attributed to cracks was subtracted from the total amount of defects.

3.2.2 Results

The results of these density measurements are shown in figure 3.4. In solid blue triangles the value measured by AOI is given, the hollow black square represent the corrected value or the pit density. The horizontal red lines are the average pit densities for the entire wafer.

One can quickly see that at higher pressure the average pit density decreases. Sample R2 has nevertheless a similar density as the low pressure samples. Measurement of another similar sample produced density values close to the values of R1, so the high values of R2 seem uncharacteristic, probably because of instabilities in the different growth run, and are disregarded. Nonetheless they are shown here for completeness. Then one can see that the density drops with an increase in pressure (and consequent decrease in carbon concentration) from 3.1-3.4 mm^{-2} to 1.1 mm^{-2}, i.e. by a factor $3/pm0.7$. Moreover the pentane doped samples have pit densities close to zero, 0.08-0.14 mm^{-2}. Relative to R sample this is a decrease by factor $10/pm5$. Relative to the A samples the density decreases by a factor 30±10. It has to be said however, that in the pentane doped samples a considerable amount of cracks was found. The large difference between the defect density and pit density at the center of sample M0860-4 is caused by these cracks. Important to note is that this not necessarily means that there are a lot of cracks in this region, but that most of the points found by AOI are making up (part of) a crack, as illustrated in figure 3.2B.

Another observation is the decrease in pit density with increasing distance from the center. This suggests that at the center of the wafer the stress is highest, requiring more stress relief in the form of defects. This difference in defects per region is nicely illustrated in the defect density map, figure 3.2C. Considering that the correction is roughly equal for all regions, this can also be used to illustrate the pit density. Since this is the case for roughly all samples, pressure and dopant type do not seem to influence this phenomenon. Therefore it is not discussed in further detail.

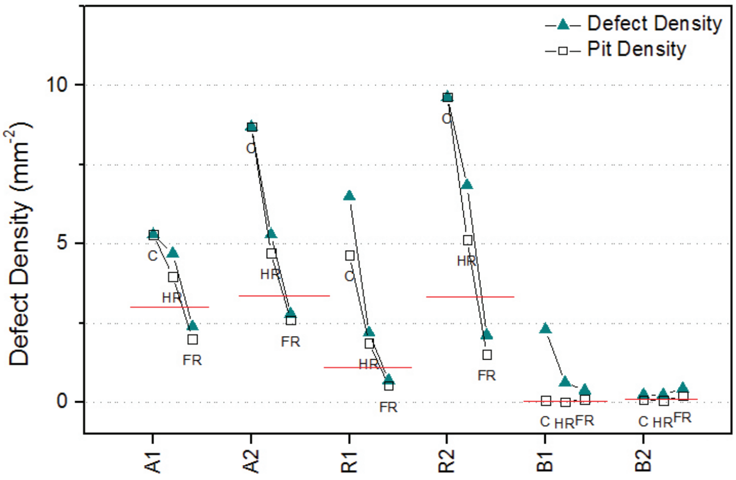

Figure 3.4: Defect density, as measured by AOI, and pit density, through correction using SEM observations, of the different samples. The separate regions are marked (C for center, HR for half radius and FR for full radius). The red horizontal lines represent the average value over the entire wafer. The error margins are 10% of the value.

Chapter 4

Pit morphology

In the previous chapter the effect of different growth parameters on the pit density was discussed. This density is not the only important aspect of the pits, the pit morphology also bears crucial information, helping to get insight in the formation mechanism of V-pits.

4.1 Pit diameter

The diameter of the pit is determined using SEM. Images of the top view of the pits are made and later on the diameter of the pit is measured using pixel counting software (ImageJ). The results of the diameter and depth measurement are presented in figure 4.1. below.

The error margins in figure 4.1 represent the standard deviation, which is significantly larger than the error measuring the diameter. For the sample R1 and R2 the standard deviation is significantly lower, although it should be noted that for all regions in samples R1 and R2 one outlier[i] was removed. Looking at the difference in diameter one can clearly see that the non-intentionally doped samples have significantly smaller pits, their average at 0.36 μm. The carbon doped samples are on average a factor 3.5±1.5, with an average of 1.25 μm for samples A and 1.18 μm for samples B. Pressure itself seems to

---

[i] The outlier was a pit with uncharacteristically big diameter, affecting the standard deviation unrepresentatively. Removing the outlier decreased the standard deviation by a factor 3-10, justifying their removal.

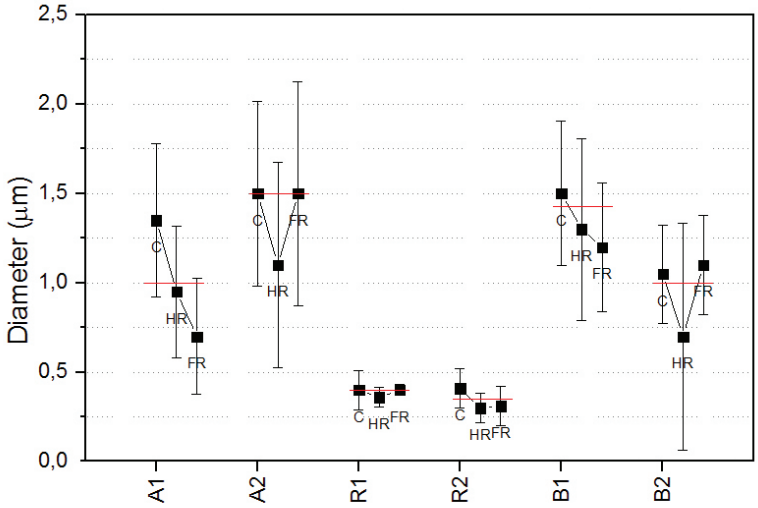

FIGURE 4.1: Average diameter of the pits for the different samples. The separate regions are marked (C for center, HR for half radius and FR for full radius). The red horizontal lines represent the average value over the entire wafer.

have no significant influence (since both low pressure carbon doped and high pressure carbon doped samples have similar diameters).

4.2 Pit facets

Another distinction between samples can be made using the pit orientation. There are two main planes along which the side facets of a hexagonal pit can be oriented, the a-plane and the m-plane, as mentioned earlier in section 2.4.1. Therefore the pits can be divided in a-oriented pits and m-oriented pits. The difference between the two pits is an apparent rotation of 90° (in fact it is a 30° rotation, the apparent rotation includes the 60° rotational symmetry). For a dodecagonal pit, exhibiting 12 side facets, the side facets are equally divided in a-oriented and m-oriented facets. These pits are from now on termed mixed pits. In order to compare the morphology of the pits to literature (for example on surface energy) the orientation of the pits is not enough; the crystal planes of the side facets should be known. From the initially used top view however one can only specify that the side facets are oriented along the a- or m- plane, i.e. the facets can be only defined as $\{1\bar{1}0x\}$ and $\{11\bar{2}y\}$, with x and y two unknown numbers. Therefore in order to define the exact crystal plane of the side facets, the angle of the pits should be measured, as will be done in paragraph 4.3.

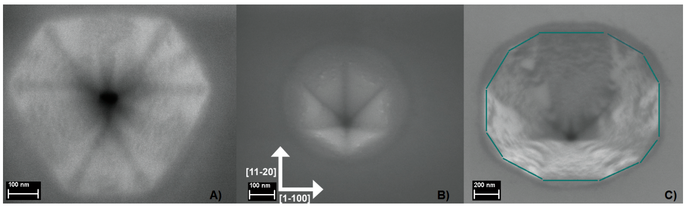

FIGURE 4.2: SEM images of the different possible orientations of V-pits. A) a-oriented pits. B) m-oriented pits. C) mixed pits with a dodecagonal shape.

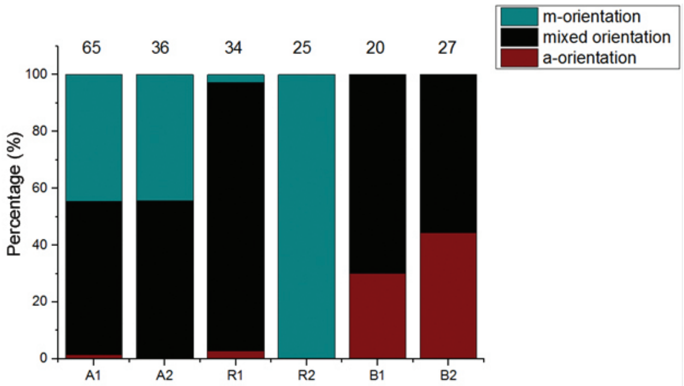

FIGURE 4.3: Distribution of the different types of orientation of the pits for the different samples. The numbers on top of the bars represent the total amount of pits characterized for the sample.

All three kinds of orientations are found in this research. The pentane doped samples exhibit mainly a-oriented pits (see figure 4.2A) and mixed pits (figure 4.2C), with a distribution (a:m:mixed) of 18:0:29. The non-intentionally doped samples show almost exclusively m-oriented pits (figure 4.2B); the distribution is 1:51:8. The precursor doped, low pressure samples show both m-oriented and mixed samples, distributed 1:35:55. These distributions are depicted in figure 4.3 to allow for a more insightful comparison.

The rotation of the pits in pentane doped samples is not a result of the higher pressure, since the non-intentionally doped samples at high pressure do not exhibit this rotation. The introduction of pentane to the system is most likely the cause of the pit rotation. Although the term rotation is used, it is important to note that the pit not actually turns; there is a difference in growth rate of side facets, preferring on orientation over the other. The orientation of the pit also appears to be linked with the pit diameter. An a-oriented pit is on average 700±190 nm in diameter, an m-oriented pit 390±180 nm and a mixed pit 1200±350 nm. Figure 4.4 is a rescaled version of figure 4.2 to illustrate this relative size.

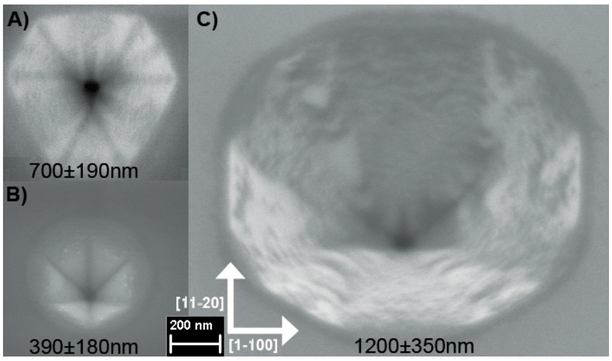

FIGURE 4.4: SEM images illustrating the difference in typical size between the different pit orientations. A) a-orientation. B) m-orientation. C) mixed pit. The sizes presented in this figure refer to the average size of all pits of the same orientation, not the specific pit shown (although the specific pit size of the shown pits does not differ much from this average).

4.3 Pit angle

As mentioned in the last paragraph the crystal plane of the side facets is of interest. In order to determine this plane, i.e. the x in $\{1\bar{1}0x\}$ and y in $\{11\bar{2}y\}$, the angle between the side facet and the surface (the c-plane) is measured. From literature the most likely facets (see table 4.1) and their angle with the c-plane (the top surface of the structures in these experiments) are known. Since the pits for samples A1, A2, R1 and R2 are m-oriented, their angles are compared with literature values for s_m- and r_m-plane. Sample B1 and B2 exhibit predominately a-oriented pits, so their angles are compared to the s_a- and r_a-plane.

4.3.1 Measurement by scanning electron microscope

The angle is not measured directly, but via the depth and diameter of the pit. Clearly one cannot measure the depth from a top view (without knowing the angle of the side facets). By tilting the wafer, the bottom of the pit and the center of the pit (the point

TABLE 4.1: Common crystal planes listed with their official names, their nickname in this thesis and the angle they make with the c-plane.

Plane	{0001}	$\{1\bar{1}00\}$	$\{1\bar{1}01\}$	$\{1\bar{1}02\}$	{11-20}	$\{11\bar{2}1\}$	$\{11\bar{2}2\}$
Official name	c-plane	m-plane	s-plane	r-plane	a-plane	-	-
Nickname	c-plane	m-plane	s_m-plane	r_m-plane	a-plane	s_a-plane	r_a-plane
Angle with c-plane (°)	-	90	61.9 [a]	43.19 [b]	90	72.91 [b]	58.41 [c]

[a] Retrieved from [94]
[b] Retrieved from [95]
[c] Retrieved from [96]

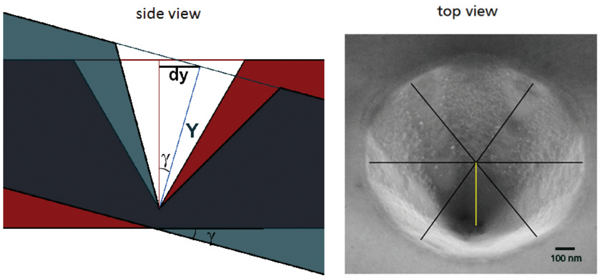

FIGURE 4.5: Tilting of the sample allows for calculation of the depth of a pit. In the side view the red parts represent the untilted sample and the blue parts the tilted sample. γ is the tilt angle, dy the apparent shift of the bottom (represented by the yellow line in the top view, and Y the depth of the pit.

where the lines connecting opposite facets intersect) shift with respect to each other and one can calculate the depth with simple trigonometry (see figure 4.5).

Measuring the apparent distance between the bottom of the pit and the center of the pit (the yellow line and dy) and the diameter (D), the facet angle (α) of the pit is:

$$\alpha = tan^{-1}\left(\frac{2dy}{D \cdot sin\gamma}\right) \tag{4.1}$$

with γ the tilt angle of the wafer (see appendix B.2 for a derivation). The measurement of these distances is done using a simple software program (ImageJ) which can count pixels. Using the scale bar, which is automatically recorded for each image taken, it is straight forward to determine the distances. For some of the non-symmetric pits $D/2$ is not accurate and is replaced by the horizontal component of the side facet. These non-symmetric pits also proof to be difficult in determining the center of the pit, as the lines connecting opposite facets do not cross in one point. The error in this measurement is mainly attributed to the inaccuracy in exactly finding the center of the pit and the bottom. This inaccuracy is however within the statistical deviation of the difference in angle in the pits. The standard deviation is therefore chosen as error margin, similarly to the earlier measurements.

4.3.2 Measurement by focused ion beam

A more direct approach on measuring the opening angle of the pit is making a cross section of the pit and directly measuring the angle. This can be done by using a focused

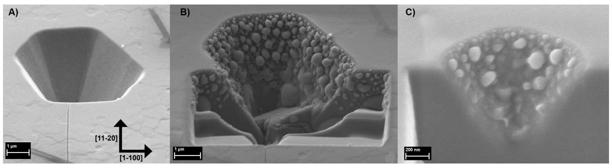

FIGURE 4.6: SEM images of A) Pit before milling with FIB. B) Pit after milling. The material that is cut out deposits on the side walls of the pit, forming drops. C) Focusing difficulties leading to blurred cross section.

ion beam[ii] (FIB) to mill half of the pit (and some extra material to be able to observe the pit). This process is briefly shown in figure 4.6.

This method however is much more time consuming and not much more precise. The great difficulty with these cross sections is focusing, leading to blurred images of the cut line of the side facets (figure 4.6C). This eventually made measuring the opening angle (done with the same software program ImageJ) susceptible to a similar error margin as tilting the wafer. Tilting the wafer was thus chosen as the preferred method, since it is significantly less time consuming.

4.3.3 Results

The results of the angle measurement by tilting the sample in the SEM are shown figure 4.7.The figure shows a large error margin for nearly all samples and regions. This error margin is, similar to the diameter measurements, defined as the standard deviation of the angle of different pits. Even with these large error margins a clear deviation from literature values for samples A1, A2, R1 and R2 is found. Voronenkov et al.[40] give an explanation for this observation: during growth in the c-direction the side facets of the V-pit grow along, due to diffusion of atoms into the pit and adsorption of atoms at the surfaces. A difference in growth rate between the side facets and the c-direction decreases the angle, eventually closing the pit. When applied to these measurements one can therefore conclude that samples A1, A2, R1 and R2 originally exhibit s_m-plane side facets, which are partly filled with additional growth material later on. A similar observation can be made for samples B1 and B2, where the average value of the facet angle is lower than the value from literature for an r_a-plane (and so far below the s_a-plane that this value from literature is not shown in the graph).

[ii] A focused ion beam uses high energy gallium ions to bombard the surface. This way one can locally remove material via sputtering, a process which is commonly named milling.

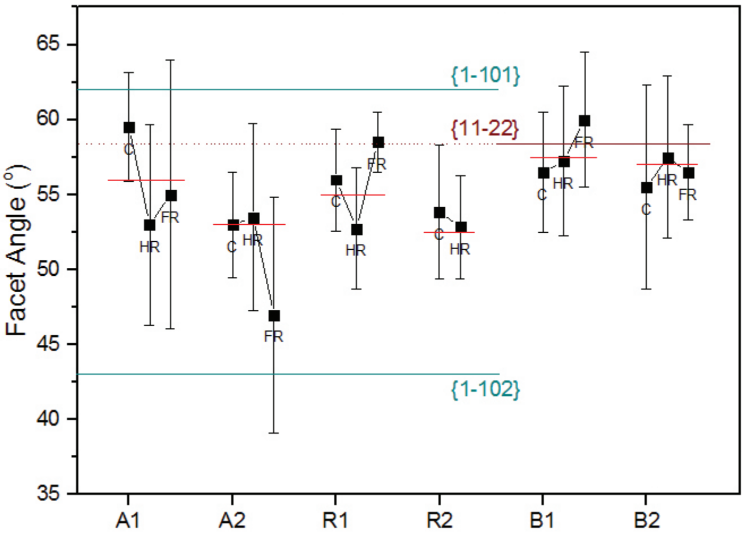

FIGURE 4.7: The facet angle of the V-pits for the different samples. Long horizontal lines represent the theoretical value of the facet angle of crystal planes.The separate regions are marked (C for center, HR for half radius and FR for full radius). The red horizontal lines represent the average value over the entire wafer. During the measurement of FR at sample R2, technical difficulties with the SEM resulted in blurred images, which made it too difficult to measure the angle.

A second observation on this graph is the absence of correlation between the position on the wafer (center, half radius or full radius) and the angle. Combining this with the large standard deviation one might say that there is no evidence of the facet angle of the pit depending on the position on the wafer.

4.4 Pit depth

To complete the picture, figure 4.8 gives the pit depth for the different samples. With the facet angle and the diameter already known, it does not provide a lot of new information. Therefore it is chosen to only present the average depth of the samples. One can see that the n.i.d. samples have more shallow pits (0.16-0.25 $/mu$m) than the doped pits (0.57-0.8 μm), an increase of a factor 3.5±1.5. This indicates that the pits of non-intentionally doped samples originate later on in the growth process. The depth can obviously be linked with the layer structure, so indicated on the y-axis of figure 4.8 are the different layers. With this added detail one might see that the origin of the pits for the doped samples is found in a doped layer. Not all origins, however, necessarily lie directly beneath the V-pit (at the tip of the inverted pyramid), as will be shown in chapter 5. More on the implications of this in chapter 6.3.

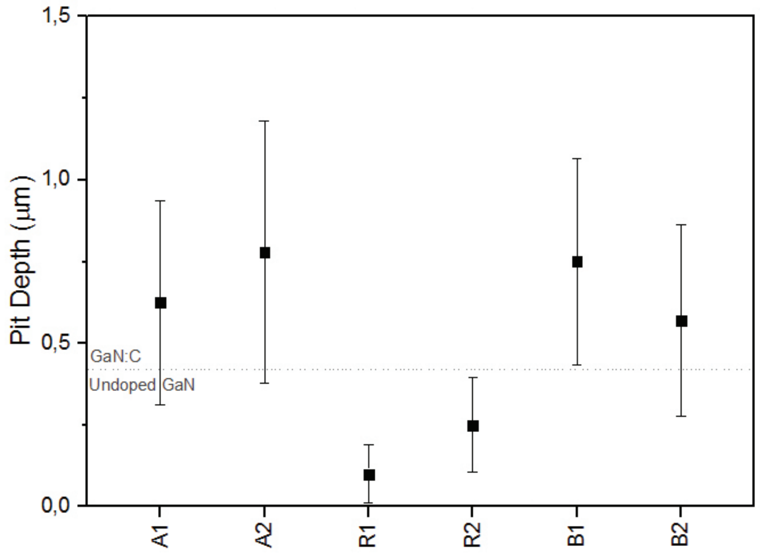

FIGURE 4.8: Depth of the different pits. The horizontal dotted line indicates the interface between the undoped GaN and doped GaN layer.

4.5 Summary

With all the results presented it is now possible to discuss the overall influence of the different parameters on pit density and morphology. In table 4.2 an overview of the (rounded) results is given.

From this table one can see that a higher pressure (samples R and B) decreases the pit density. Carbon doping of the samples (A and B) increases pit diameter and depth. These larger pits exhibit dodecagonal shapes or mixed orientations. Using pentane as dopant (samples B1 and B2) leads to the lowest pit density, but also induces crack formation. Moreover the pentane doped samples show an a-orientation.

TABLE 4.2: Overview of the resulting pit density and morphology for the different samples

Sample	**Pit density (mm^{-2})**	**Cracks**	**Pit diameter (μm)**	**Pit orientation**	**Depth (μm)**
A1	3	No	1	m- and mixed	0.6
A2	3	No	1.5	m- and mixed	0.8
R1	1	No	0.4	m-oriented	0.2
R2	3	No	0.3	m-oriented	0.3
B1	0.1	Yes	1.4	a- and mixed	0.8
B2	0.1	Yes	1	a- and mixed	0.6

Chapter 5

Pit origins

In the previous chapters the influence of the growth parameters on pit density and morpoholgy is treated. These measurements are limited to observation of the surface, and therefore only explore the result of pit formation. Equally interesting is investigation of the origin of pit formation. Possible causes of this V-pit formation are discussed in this chapter.

In order to investigate the origins of the pit formation, TEM measurements were done on selected pits for sample A (low pressure and precursor doped) and sample B (high pressure and pentane doped). These TEM measurements were carried out by Andreas Graff, Susanne Hübner and Michel Simon-Najasek at the Fraunhofer Center for Applied Microstructure Diagnostics, part of the Fraunhofer Institute for Mechanics of Materials in Halle, Germany. It is important to note that these measurements concern two single pits, which is statistically speaking very limited, but unfortunately induced by time and financial constraints. These pits were selected for their symmetric shape and typical size. These pits might not be more common than asymmetric pits, but the symmetry in the pits suggests a more fundamental cause than asymmetric pits, which exist in a multitude of shapes. Furthermore one of the pits is found on a separate, low pressure, precursor doped sample from the same run as sample A1 and A2. This sample is not investigated on pit density or morphology, so no characteristics, such as predominant orientation or pit density, of the sample are available. Nonetheless these characteristics are assumed to be similar to the thoroughly investigated samples A1 and A2.

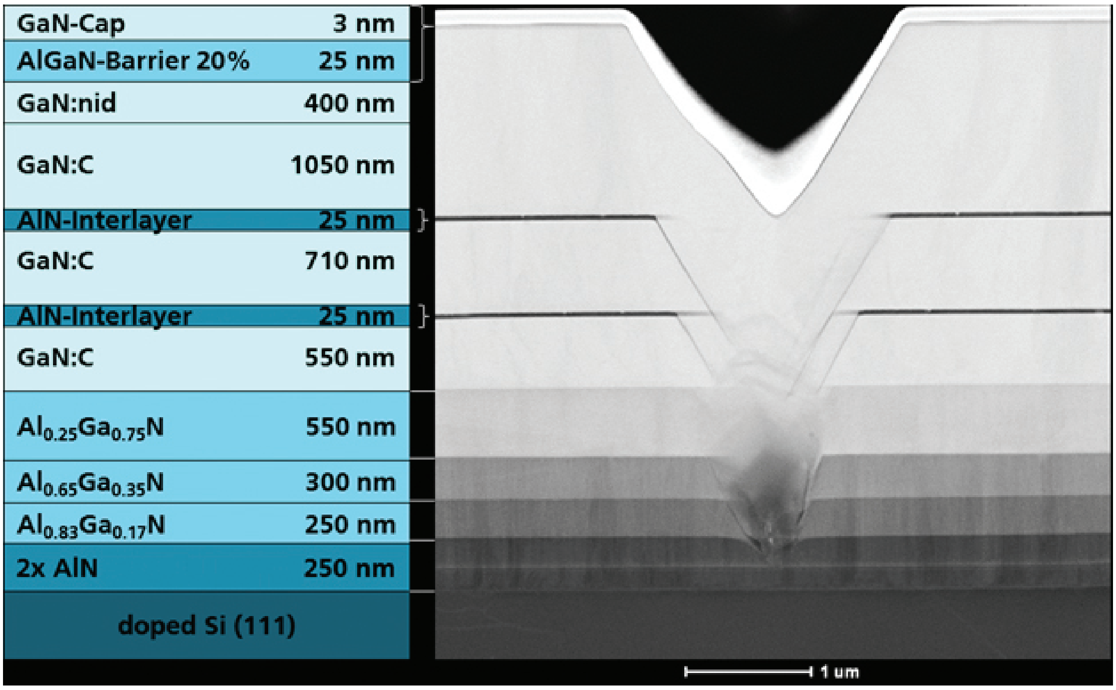

FIGURE 5.1: Schematic buffer structure and high-angle annular dark-field STEM image of the typical HEMT structure used in these experiments. The particle lies at the AlN regrowth interface.

In figure 5.1 one can see one of the TEM images from the measurements (earlier presented in section 3.1 to introduce the HEMT structure). This image clearly suggests a cause of the V-pit formation, a particle directly below the V-pit. This particle seems to originate from the regrowth interface of the AlN seeding layer, which suggests that a particle fell down on the template structure before the growth of the HEMT structure. By means of energy-dispersive X-ray spectroscopy (EDX) the composition of this particle can be measured, as shown in figure 5.2. These measurements indicate that the particle mainly consists of AlGaN, with a some oxygen and carbon contaminants at the surface of the particle. This suggests that this particle is not a foreign particle, but was present at the ceiling after grown during earlier runs, therefore exposed to gallium, and fell down on the template before the seeding layer growth, possibly during heating of the reactor.

With the particle on the template, the subsequent grown HEMT layers are affected by its presence. Near the particle the layer thickness decreases, while at the same time material is growing on top of the particle. This greatly influences the growth front of the layers, as illustrated in figure 5.3. At the last graded buffer layer the growth front is almost recovered, but not in time for the GaN growth. At this first GaN layer the growth front dramatically alters. The lateral growth needed to close the pit is lower

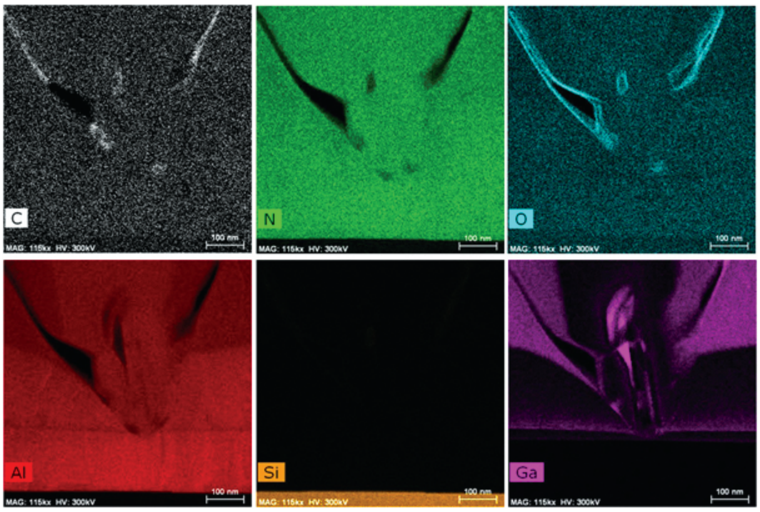

FIGURE 5.2: EDX measurement of the particle found at the regrowth interface of the AlN layer directly beneath the V-pit. The letters represent the atoms depected. Scale bars are 100nm long

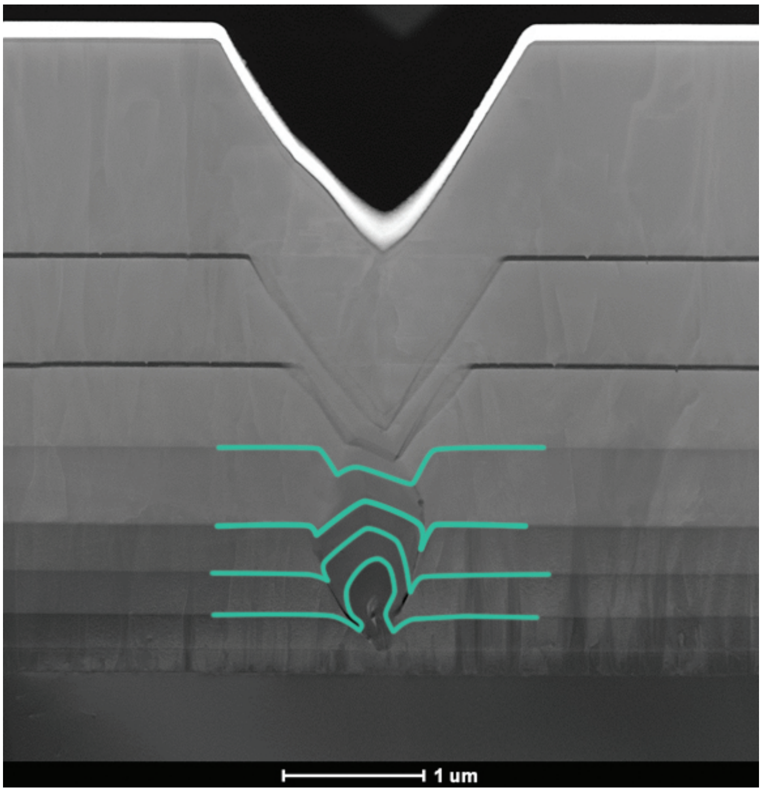

FIGURE 5.3: High-angle annular dark-field STEM image depicting the disturbance of the growth fronts of the graded buffer layers by the particle.

than the vertical growth, promoting growth of a V-pit. In order to close the pit, i.e. to restore the growth front to a horizontal line, an increased lateral growth is needed.

Relating lateral growth to closure of a V-pit, one can propose a correlation between lateral growth and pit density. Namely, a high lateral growth restores the growth front

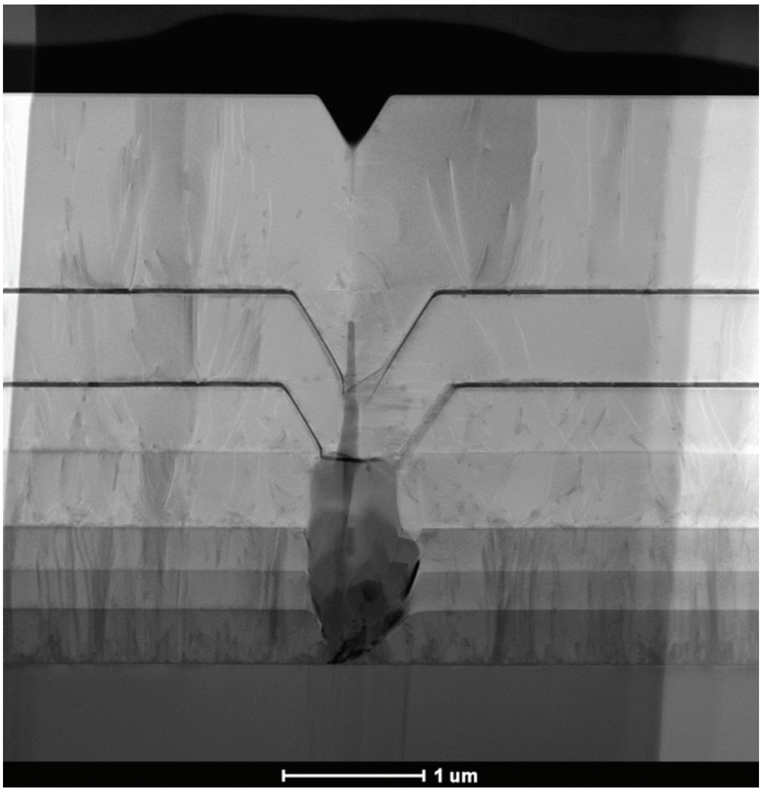

FIGURE 5.4: High-angle annular dark-field STEM image of the origin of a V-pit in a pentane doped sample.

more easily and therefore closes pits, which eventually is seen as a lower pit density. Applying this mechanism to compare pits in sample A and sample B, one can predict two things about a V-pit in sample B. Firstly one can say that in sample B the lateral growth rate is higher, since it has a lower pit density. Secondly it predicts the cause of the V-pit. Since the V-pit still remains, even with the higher lateral growth rate, the particle (and subsequent disturbance of the step graded buffer) causing pit formation, must be larger than in sample A. Looking at the TEM image for a pit in sample B (figure 5.4) both of these predictions hold. Firstly the increased lateral growth is clearly visible as a larger distance between the side facets of the pit marked by the dark AlN interlayer. Measuring the relative lateral growth rate, the lateral growth rate divided by the vertical growth rate, the increase in lateral growth rate can be quantified. For sample A this relative lateral growth rate is 0.25±0.04, whereas for sample B this is 0.67±0.04, an increase of a factor 2.7±0.5. Secondly one can clearly see that the particle, in this case originating at the silicon substrate, and subsequent disturbance of the step graded buffer, are bigger. Unfortunately EDX measurements are not (yet) available to measure the contents of the particle.

Since these measurements entail only two pits, the drawn conclusions are possibly not statistically stable. To summarize these speculations, a proposed formation mechanism is presented below.

1. A particle falls on the template or substrate.
2. The ordered, vertical growth of subsequent layers is disturbed by the presence of the particle.
3. s_m- or r_a-planes are grown as alternative to the growth in the c-direction (if the growth front not recover before the GaN layers grow).
4. Lateral growth fills the pit, decreasing the facet angle, on its way to close the pit.

Chapter 6

Discussion

The measurements performed in this research suggest a significant influence of doping on the pit density and pit morphology. Five significant trends were found and will be discussed here. To summarize, a model describing the formation and closure of V-pits is proposed. After that a speculative, improved model is presented.

6.1 Decrease in pit density

The first observation is the decrease in pit density at high pressure. From the TEM measurements, discussed in chapter 5, one would say that the lateral growth rate (LGR) increases with pressure, shutting the V-pits. Habel [21] and Hiramatsu et al.[48] however suggest that a higher pressure promotes the growth of side facets, either s_m- or r_a-plane, i.e. the growth rate in c-direction increases with pressure, in the range of 100-200 mbar. This would mean that at a higher pressure, V-pit growth would be promoted, contradicting the findings in these experiments.

Looking at another important growth parameter, temperature, Habel and Hiramatsu do find increased LGR for higher temperature. Moreover this effect is stronger (factor 4 over 100 °C) than the decrease in later growth rate by pressure (factor 1.2 over 100 mbar), suggesting that the temperature effect is dominant in the growth rate [21]. Even though for all samples the set reactor temperatures effectively agree (with a maximum variation of 10 °C), the more important surface temperature turns out to be different. All surface temperatures are lower than the reactor temperature, but at low pressure this temperature drop is even greater (see table 3.1 at page 34). The cause of the temperature difference between the reactor temperature, measured beneath the reactor at the heater, and the surface temperature is caused by the cool gas, i.e. reactants and hydrogen carrier gas, flowing over the samples. The gas flows at the different pressures are optimized for optimal growth and different between the samples. Therefore the cooling effect differs between the two reactor pressures, resulting in different surface temperatures. This difference in surface temperature then might explain the difference in LGR and therefore the difference in pit density. Applying the earlier found correlations to these sample preparations, with a temperature difference of 70°C and a pressure difference of 165 mbar, the temperature contribution to the change in lateral growth rate is a factor 2.4 and the pressure contribution a factor 2.

The further decrease in pit density by pentane doping can be explained by an additional increase in LGR due to carbon impurities, as found for magnesium [97] and silicon [98] impurities. This same increase should be found for the high pit density, precursor doped, low pressure samples however, since they have a similar impurity concentration as the pentane doped samples. Therefore this effect seems significantly smaller than the increase in LGR by a change in temperature. To summarize the influence on lateral growth: low pressure samples have a small LGR due to lower surface temperature and a small additional LGR due to the carbon doping. The n.i.d. samples have a high LGR due to a high surface temperature and no additional LGR due to doping. The pentane doped samples have a high LGR due to high temperature and an additional LGR due to carbon doping.

This trend for the LGR is supported by the TEM measurements comparing the pentane doped sample with the precursor doped sample. The later growth was a factor 2.7±0.5 higher for the pentane doped sample. Since the carbon concentration for both samples is considered equal, the increase in LGR can be attributed to an increase in temperature and pressure (and the presence of pentane). As mentioned before, temperature and pressure have opposing effects on the lateral growth rate. Additional measurements separating the two parameters can be done to distinguish between the two effects. Such measurements could profit from a different control system of the reactor, keeping the surface temperature fixed rather than the reactor temperature. This would allow variation of the surface temperature at a constant reactor pressure.

Additional measurements can potentially find evidence for the contribution of carbon doping to the LGR. By fixing the temperature and varying the carbon concentration the influence of carbon doping can be found. Since growth temperature and carbon concentration are closely related, as earlier mentioned in section 2.4.2, it is impossible for the precursor doped samples to fix either temperature or carbon concentration and change the other. Pentane doped samples have an independently controlled carbon source (changing the amount of pentane present in the reactor), making them suitable to fix one parameter and change the other. Therefore any experiments exploring the separate influence of growth temperature and carbon concentration should be done using pentane doped samples.

6.2 Crack formation

Another important observation is the occurrence of cracks for the pentane doped samples. Since these cracks are out of the scope of this work, no detailed analysis of their appearance is carried out. Their formation however can give some insight into the formation of pits. In appendix A, a possible hint as to why these cracks are formed is given, through analyzing the curvature of the samples.

6.3 Increase in pit diameter and depth

The third observation is an increase in pit diameter (and depth) of a factor 3.5±1.5 for doped samples. The increased depth suggests that the V-pits originate in the carbon doped layers, and that the introduction of carbon induces more irregularities and dislocations than in n.i.d. samples. Therefore carbon can induce a higher probability of disrupting the vertical growth, which eventually causes the V-pit formation (no particle is involved). The bigger diameter then follows from a longer growth time, since it originated earlier, of the V-pit with its inclined sidewalls. Additionally a longer growth time can expose the V-pit to lateral growth for a longer time, decreasing its diameter. This suggests that the origins of the V-pit lie even deeper, since the lateral growth decreases the large diameter caused by its deep origin. In all cases there is a possibility of a V-pit originating at a particle. The size of such a pit is then a combination of the size of the disruption caused by the particle and the lateral growth rate, as explained in chapter 5.

6.4 Pit orientation

The fourth observation is an apparent rotation of the pits for pentane doped samples. The n.i.d. samples and trimethyl-doped samples exhibit s_m-plane side facets, whereas the pentane doped samples show r_a-plane side facets. In literature the s_m-plane is predominantly found, so one might consider this plane as the normal facet plane. This suggests a change in either growth rate or surface energy for the pentane doped samples.

Following Northrup and Neugebauer [47], the surface energy of GaN planes can be lowered by inclusion of indium atoms. Something similar is possibly happening with carbon atoms. Surface energies are very complex and dependent on a multitude of parameters, as mentioned in Li [44]. Possibly the combination of high pressure and temperature and high carbon concentration lowers the surface energy of the r_a plane, to make it more energetically favorable than the s_m-plane. Redoing the calculations by Northrup and Neugebauer for carbon, instead of indium, should point out if carbon can change the surface energy in a similar fashion as indium and might give more insight into the mechanisms at work.

6.5 Big pits exhibit mixed orientation

Lastly the orientations appeared to have a correlation with size. Especially the large pits (around 1 μm) appeared to have a dodecagonal shape, or a mixed orientation. This can be explained by energy minimization; even though the additional planes have a higher surface energy, their introduction leads to a decrease in overall surface area, since they offer a 'shortcut'. Thus it leads to a decrease in total surface energy. A similar observation, the introduction of a r_a-plane between two neighboring s_m-planes, is also found by Sun et al.[99].

For the observation that r_a-plane pits are larger than s_m-plane pits, no explanation is found, partly because of the scarcity of reports on r_a-plane pits in literature. However one can speculate on a possible mechanism that incorporates these findings, as is done in section 6.7.

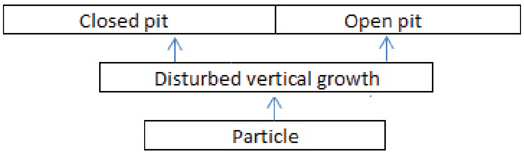

FIGURE 6.1: Model describing pit formation and closure.

6.6 Proposed model

To summarize, a mechanism describing formation and closure of V-pits is proposed based on these observations (see figure 6.1).

1. A particle falls on the template or substrate.
2. The particle disrupts the vertical growth. s_m-planes (for precursor doped and n.i.d. samples) or r_a-planes (for pentane doped samples) are grown as alternative to the c-growth, i.e. a hole with crystallographic lateral facets (V-pit) is created.
3. Lateral growth fills the pit, depending on the lateral and vertical growth rates shutting or opening the pit. High surface temperature samples have a higher LGR, therefore more V-pits get shut and the pit density decreases. Carbon doping further increases the LGR.

6.7 Speculative improved model

Not all observations in this work can be explained by this model, for example the low standard deviation for the pit diameter at the n.i.d. samples and the larger size of the s_m-plane pits compared to the r_a-plane pits. Relating this unexplainable observation to literature, one can speculate on an improved model, that additionally incorporates findings from other works in literature. However, without critical, experimental evidence this model remains purely speculative. Thus, it cannot be stressed enough, this enhanced model is only partly based on evidence in this work and includes unfunded assumptions. The enhanced model (see figure 6.2) is presented here merely to build a framework and give suggestions for further research relating to this subject.

The first addition to the model is an extra category of causes for V-pit formation. As mentioned in section 2.4.2, there are other causes for V-pit formation than particles.

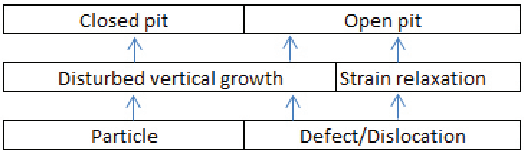

Figure 6.2: Speculative improved model of the formation and closure of V-pits

These other causes (e.g. stacking faults, threading dislocations and inversion domain boundaries) can be categorized as defects. V-pits originated by such defects are not observed in these experiments, so in order to confirm this model, they should be observed first. The defects or dislocations can cause either a disturbance in the vertical growth or induce pit formation through a different mechanism, as will be explained below. As can be seen in figure 5.1 in chapter 5 (as vertical lines that reach the surface), there are defects that do not cause a V-pit. This is also observed in literature [39][50], but no explanation, as to why they do not cause a V-pit, is given.

The second addition is another incentive, or mechanism, to form V-pits. In the present work, the mechanism found is a disturbance in the vertical growth by foreign particles, but in literature there is mention of another mechanism, strain relaxation. As mentioned earlier in section 2.4.2, the driving force for pit formation can be a “reduction in energy achieved by avoiding the accumulation of strained material in the region near the core of the dislocation.” [47] This mechanism could explain why the small pits at n.i.d. samples did not grow shut through lateral growth; shutting the pits would defeat the purpose of the formation, i.e. it is energetically unfavorable.

Song [58] additionally explains that the strain relaxation occurs at a critical thickness of the buffer layers. This might explain the relatively small standard deviation of the pit size for the n.i.d. samples; the pits start developing at the same time, or more precisely the same thickness. If TEM measurements of these typically sized pits show that there are no particles involved in the pit formation, this might be considered evidence to support the strain relaxation mechanism.

Furthermore it is stated that the reduction in strain energy is accomplished at the expense of increased surface energy, and the size and shape of the pit is affected by the surface and dislocation energetics.[47] This gives a hint as to why the r_a-plane pits are bigger than s_m-plane pits; their surface energy could be lower. As mentioned before, these surface energies are hard to predict, so additional calculations are needed to explain the size difference in more detail.

Chapter 7

Conclusion

In conclusion the combination of AOI tools and SEM allowed detailed measurements of the V-pit density and morphology on three different species of samples. A clear influence of the growth parameters, pressure and temperature was found.

Using the freedom provided by pentane as external C doping source, higher growth pressure can be achieved. Increasing the pressure by 165 mbar and consequently the surface temperature by 70°C, lowers the V-pit density by a factor 3±0.7. Adding pentane further decreases the density a factor 10±5. TEM measurements attribute the decrease in pit density to an increase in lateral growth. This increase is quantified to a factor 2.7±0.5 over 70°C and 165 mbar (and the introduction of pentane). Relating this finding to literature it seems more likely that the increased lateral growth is a result of the increased surface temperature than of the increased pressure.

Increasing the carbon concentration, either through TMG or adding pentane, results in an increase of the average pit diameter and pit depth by a factor 3.5±1.5.

Adding pentane changes the crystal orientation of the side facets of the V-pits from s_m-planes to r_a-planes, which is probably caused by a decrease in surface energy due to the high temperature, pressure and carbon concentration.

Based on these findings a formation mechanism is proposed. However the small standard deviation of the pit diameter for n.i.d. samples and the larger size of the s_m-plane pits compared to the r_a-plane pits cannot be explained by this formation mechanism. Additional experiments are needed to support proposals by an enhanced model that possibly explains the remaining observation and incorporates findings in other works in literature.

Chapter 8

Recommendations

Based on this work several recommendations for further research can be proposed. Some of these recommendations are already mentioned in the earlier sections of this work. They are listed here again to offer a complete overview.

A first recommendation is an expansion of the number of samples and pits measured. The trends found for the growth parameters apply to the samples used, but these are only six samples. Moreover they apply to only a few tens of pits. Clearly it would be extremely helpful to record data on more pits and more samples per run. Since these runs might be susceptible to fluctuations, multiple runs would even further improve the stability of the trends.

Where the density and morphology measurements using SEM and AOI are a great indicator of the result of growth parameters, the TEM measurements are a great source of information on the history and formation of a pit. Such a TEM measurement is a costly experiment, both in time and financially. However the measurement provided a load of information on the possible origin and formation mechanism of a V-pit. Since this only concerns two pits, it is difficult to statistically correctly extrapolate the findings of this measurement to all pits. Running the same measurement for multiple pits can increase the statistical stability of the predictions made based on these first two measurements.

Both the formation mechanism and the ultimate result (expressed in density and morphology) can thus be staticsally improved. To find out more about the result of growth parameters, investing time in increasing the number of data points with the AOI and

SEM method is recommended. For more information on the formation mechanism, investments in more TEM measurements should be made.

Another great source of information on pit and crack formation is hidden in the curvature of the structure. An attempt to grasp the implications of this curvature was done alongside the experiments presented in this work (see appendix A for a more detailed discussion), but no definite conclusion which could contribute to the findings in this thesis could be drawn. Further investigating this theme is highly recommended, since I believe it gives insight in the evolution of stress relief.

As mentioned before, temperature and pressure have opposing effects on the lateral growth rate. Additional measurements separating the two parameters can be done to distinguish between the two effects. Such measurements could profit from a different control system of the reactor, keeping the surface temperature fixed rather than the reactor temperature. This would allow variation of the surface temperature at a constant reactor pressure. These different samples can then be measured for the effect on the pit density, by SEM and AOI, and on the lateral growth rate, by TEM.

Additional measurements can potentially find evidence for the contribution of carbon doping to the LGR. By fixing the temperature and varying the carbon concentration the influence of carbon doping can be found. Since growth temperature and carbon concentration are closely related, as earlier mentioned in section 3.1.4, it is impossible for the precursor doped samples to fix either temperature or carbon concentration and change the other. Pentane doped samples have an independently controlled carbon source (changing the amount of pentane present in the reactor), making them suitable to fix one parameter and change the other. Therefore any experiments exploring the separate influence of growth temperature and carbon concentration should be done using pentane doped samples. These different samples can again be measured for the effect on the pit density, by SEM and AOI, and on the lateral growth rate, by TEM.

The speculative model proposed in chapter 6.7 requires additional measurements and observations to proof it right. There are other causes (e.g. stacking faults, threading dislocations and inversion domain boundaries) for V-pit formation than particles, as mentioned earlier. V-pits originated by such defects are not observed in these experiments, so in order to confirm the improved model, they should be observed first. Additionally these observations can support the strain relaxation mechanism proposed by Song [58], predicting different pits to have a uniform size. If TEM measurements of these typically sized pits show that there are no particles involved in the pit formation, this might be considered evidence to support the strain relaxation mechanism.

The rotation of the pits in pentane doped samples is attributed to a change in surface energy. As mentioned before, these surface energies are hard to predict. Typically these energies are calculated using density functional theory. Making these calculations concerning the environment (with pentane and hydrogen present) in these experiments can shed light on the cause of the rotation. Additionally the surface energy might explain the size difference between a-oriented pits and m-oriented pits, according to Northrup and Neugebauer [47].

Appendix A

Curvature

This thesis mostly described defect densities and pits. Another inherent phenomenon in heteroepitaxy is bending of the wafer. This is mainly caused by the difference in thermal expansion coefficient (TEC) between the substrate and the grown material, which during cool down after the growth process induces this bending. In this appendix some (unfinished) research is presented on curvature measurements, analyzing the bending of the wafer.

A.1 Fundamental aspects

In order to completely understand the measurements presented in this appendix, some additional fundamental aspects are covered.

Most effort in strain engineering is done to prevent this bending at cool down. However entirely eliminating bowing of the wafer is very hard, since curving at cool down is not completely predictable, since strain relaxation through pits and cracks is not completely understood. A sample with high curvature creates problems in processing; during the important photo lithography steps the wafer is put on a stepper. This stepper moves very quickly during the lithography, so the wafer needs to be attached firmly to the stepper. This is done by creating a vacuum under the wafer, but when the wafer is bend too much, this vacuum might not be strong enough to withstand the forces during rapid movement. This causes the wafer to slip, introducing errors when the wafer is illuminated with a specific pattern. Also the masks should be adjusted to obtain optimal results with highly curved wafers. For the standard IAF process on 100 mm diameter substrates, the acceptable wafer bow must be between ±70 μm, corresponding to curvature values between ±56 km^{-1}.

There are several contributions to wafer bending: a difference in lattice parameter between substrate and deposited layers (as extensively covered in section 3.1), a difference in TEC a vertical temperature gradient in the substrate, .

The vertical temperature gradient is formed when the front side of the wafer is cooled by the gasses in the reactor flowing over the surface [100]. When the heat conductivity of the substrate is low, as for example in sapphire, this can lead to a significant temperature difference between front side and back side. This leads to bending of the substrate following:

$$\kappa_{tg} = \alpha_s \frac{T_{back} - T_{front}}{h_s} \tag{A.1}$$

With κ_{tg} the curvature induced by a temperature gradient (in km^{-1}), s the TEC (in K^{-1}) of the substrate, T_{back} and T_{front} the temperature at the back side and front side respectively and h_s the thickness of the substrate. Si(111) substrates however have thermal conductivity five or six times higher than sapphire [101], so that the heat spreads much more evenly instead of building up this temperature gradient. Moreover the thermal expansion coefficient of Si is a factor 3 lower than with sapphire [100][102]. Therefore with Si substrates the curvature induced by a vertical temperature gradient is negligible.

The strain caused by a difference in TEC between the substrate and the grown materials, can be expressed as:

$$\epsilon = d\alpha \cdot dT \tag{A.2}$$

With ϵ the strain, $d\alpha$ the difference in thermal expansion coefficient and dT the temperature difference upon cool down. For GaN ($5.59 \cdot 10^{-6} K^{-1}$[9]) and Si ($2.59 \cdot 10^{-6} K^{-1}$[9]) this difference is $3 \cdot 10^{-6} K^{-1}$. As in a bi-metal this difference in expansion leads to bending of the epitaxial structure (or film) and the substrate. In case of GaN on Si this leads to tensile strain and therefore concave curvature (See figure A.1 below). This curvature can be calculated using the Stoney equation [100]:

$$\kappa = 6 \frac{M_f}{M_s} \frac{h_f}{h_s^2} \epsilon \tag{A.3}$$

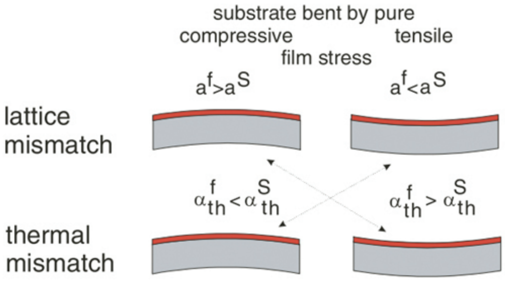

FIGURE A.1: Curvature through thermal and lattice mismatch. Reprinted from [68]

with κ the curvature, ϵ the strain (both from thermal and lattice mismatch), $M_{f,s}$ the biaxial moduli, and hf, s the thickness of the film and the substrate respectively[i]. Clos et al.[103] proposed a non-linear approach to Stoney's formula to more accurately represent the mismatch strain. For the case of GaN on Si(111)[104] this modification can be reduced to a correction coefficient c:

$$\kappa = 6c\frac{M_f}{M_s}\frac{h_f}{h_s^2}\epsilon \tag{A.4}$$

With a substrate thickness of 675 μm, $\frac{M_f}{M_s} = 1.7$ and a correction coefficient of 0.7 [104] this reduces to:

$$\kappa = 15.67 \cdot 10^3 h_f \epsilon \tag{A.5}$$

with h_f in μm[ii].

A.2 Method

The curvature of the samples used in these experiments are measured in two different ways: an in-situ curvature measurement by the EpiCurve TT Two sensor and an ex-situ bow measurement using a Tropel FlatMaster 100. The EpiCurve sensor can additionally measure reflectance oscillations, yielding the growth rate of the deposited layers, a parameter needed in calculations later on. All methods and calculations are explained in this paragraph.

---

[i] The formula makes use of the approximation $h_f << h_s$, which in these experiments is fulfilled ($4\mu m << 675\mu m$).

[ii] These values are adapted from Aidam et al.[104], who studied structures consisting of only an AlN seeding layer and a thick GaN buffer. The step-graded buffer and AlN interlayer that are used in these measurements are not included in these approximations. The very thin AlN interlayers are not likely to effect the approximation significantly and the graded buffer seems to have negligible effect as well.

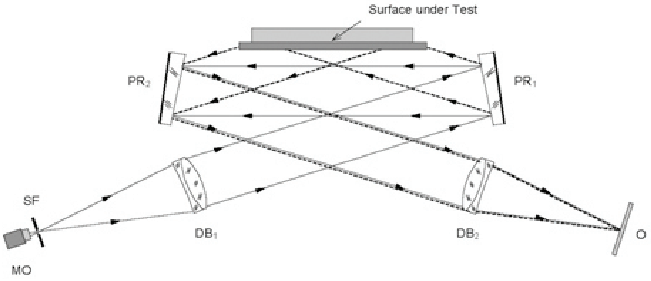

FIGURE A.2: Principle of a grazing incidence interferometer for wafer bow measurement. Reprinted from [105].

A.2.1 Bow measurement

Bending of a wafer can be expressed in two different parameters, bow and curvature. While the in-situ measurement records the wafers curvature, the apparatus used to measure ex-situ, records bow. Bow is defined as the height difference between the lowest point and the highest point of a paraboloid best fitting the wafer shape. In these experiments a Tropel Flatmaster 100 is used. This Flatmaster is a non-contact grazing incidence interferometer (see figure A.2 below)

A helium-neon laser is focused on a spatial filter (to remove aberrations), which in turn is placed in the focal point of a doublet (two lenses paired together). A prismatic beam splitter directs one beam (the object beam) to the surface under test, in this case a wafer with a thin film, and one reference beam to a second prismatic beam splitter. The object beam strikes the surface under a high incidence angle (hence the name grazing angle) in order to increase the reflectance of (normally low reflective,) unpolished surfaces [105]. The second prismatic beam splitter recombines the two beams, inducing interference. The superposed beam illuminates a CCD camera, which records the fringe pattern. These fringes are a result of a difference in phase between the two beams. This phase difference correlates with local wafer height[iii], after which the bow (heighest point lowest point of the best fitting paraboloid) is calculated. Figure A.3 presents a typical result of such a bow measurement.

As mentioned before, bending of a wafer can be expressed in two different parameters, bow and curvature. Curvature is defined as the reciprocal radius of the virtual circle(segment) that could be fitted to the curve. One can proof (see appendix B.3) that

---

[iii] Unfortunately the exact correlation is not found in literature. In section A.2.2 a correlation is given for Fabry-Pérot interferometry, which might give a clue to the correlation for this grazing incidence interferometer.

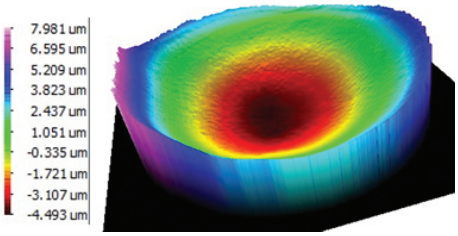

FIGURE A.3: Typical result of a bow measurement with the FlatMaster 100. The color scale indicates the height of the wafer at different locations. The best fitted parabola for this measurement, not shown in this figure, resulted in a bow of (-9 μm)

curvature κ relates to the earlier defined bow b following:

$$\kappa = -\frac{8b}{D_w^2} \tag{A.6}$$

with D_w the diameter of the wafer. Using the standard unit of curvature (km^{-1}) and bow (μm) and taking the diameter of the wafer to be 10 cm, this simply becomes:

$$\kappa = -0.8 \cdot b \tag{A.7}$$

as is found by Aida et al.[106] Using this relationship the results from a bow measurement can be converted into a curvature value.

A.2.2 Curvature measurement

In the ceiling of the MOCVD reactor chamber EpiCurve TT Two sensors are mounted to monitor the curvature during growth of all eleven 100 cm wafers. For one wafer there can be up to three different sensors, in order to measure the curvature at the center of the wafer, at half radius and at full radius. Figure A.4 shows the elements of these sensors. A laser beam is split and the two beams reflect from the wafer. A chromatic mirror directs the reflected beams into the CCD camera, while it simultaneously filters light of other wavelengths (incandescent light emitted from the wafers). Part of the reflected beams (10%) is directed by a half-mirror into a reflection compensation detector, which regulates the laser intensity. Depending on the curvature these two beams either move closer towards each other (concave wafer, example B), move away from each other (convex wafer, example C) or stay at the same distance (flat wafer, example A). The distance between the beams is a measure of the curvature.

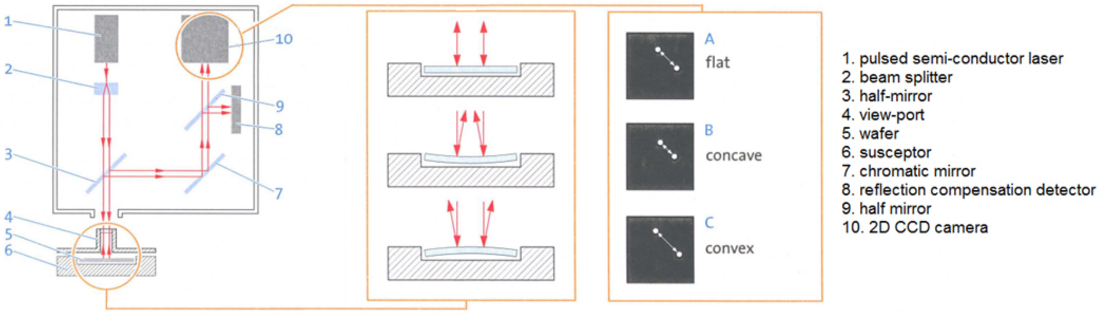

FIGURE A.4: Schematic overview of the Epicurve TT module. Adapted from the LayTec Manual, version 1.0, December 2008, D-60071 Berlin

An important difference between the bow value measurement done with the Flatmaster and the final curvature measured by the EpiTT Curve is the temperature at which the measurements are carried out. While the Flatmaster measurement is done at room temperature, the finale value of the EpiTT Curve curvature is measured at 100°C. This difference can be compensated with an additional curvature term by thermal mismatch, following equation B.2.

A.2.3 Growth rate measurement

The vertical growth rate is a key parameter in epitaxial growth. Optical reflectance is a popular method of measuring this growth rate in real time. This method (called Fabry-Pérot interferometry) uses interference patterns to deduce the layer thickness. When a beam of coherent light is incident on a thin film on a substrate, it partly reflects and partly propagates in the thin film. At the interface between the substrate and the film the same thing happens; the light partly propagates in the substrate and is partly reflected back into the thin film. At the interface between the thin film and air again the light splits (and so on). The light that reflected on top of the thin film at the first place and the light that reflected at the substrate and escaped the thin film again, interact to form an interference pattern. Whether the superposition of both beams is constructive or destructive, depends on the phase difference caused by the longer route of the beam that went through the thin film. This extra pathway is given by:

$$D = 2\, n\, d\, cos\, \theta\, tan\, \theta \tag{A.8}$$

with n the refractive index of the thin film, d the film thickness and θ the angle of incidence. This gives a maximum when this difference is an even number of half the wavelength of the light ($2nd\frac{sin\,\theta}{tan\,\theta} = m\cdot\lambda$) and a minimum when it is half a number of the wavelength of the light ($2\,n\,d\,\frac{sin\,\theta}{tan\,\theta} = (m+\frac{1}{2})\cdot\lambda$). λ in both equations is the wavelength of the light used. These oscillations are called Fabry-Prot oscillations and are seen in the reflectance of the light used to measure the curvature. This beam enters normal to the surface (see figure A.2). The deviation by curvature is only very small, so one can approximate θ by 90°. This reduces the equation to $2\,n\,d = m\cdot\lambda$ and $2\,n\,d = (m+\frac{1}{2})\cdot\lambda$ respectively. The growth rate can then easily be found from the distance between two peaks (the distance in this case is clearly a measure of time).

$$GR = \frac{\lambda}{2\,n\,dt} \tag{A.9}$$

With dt the time between two maxima or minima. The amplitude of the reflectance R is given by

$$R = \frac{I_{reflected}}{I_{incident}} = (n-1)^2 + \frac{k^2}{(n+1)^2} + k^2 \tag{A.10}$$

with n again the refractive index and k the extinction index. These indexes are material properties and therefore the amplitude of the reflectance is a measure of the composition of the layer. This could be used to determine for example the composition of the graded buffer (even though it is not done in these experiments).

A.2.4 Data manipulation

As mentioned before, one can attribute several sources that contribute to the final strain; strain by lattice mismatch (ϵ_{lm}), strain by thermal mismatch (ϵ_{tm}) and strain relaxation through defects (ϵ_{def}), such as pits and cracks:

$$\epsilon_{final} = \epsilon_{lm} + \epsilon_{tm} - \epsilon_{def} \tag{A.11}$$

Through equation A.5 strain information can be converted to curvature data: Or similarly

$$\kappa_{final} = \kappa_{lm} + \kappa_{tm} - \kappa_{def} \tag{A.12}$$

During growth of the samples used in this research, the evolution of curvature over time was measured by the EpiCurve TT sensors. This allows detailed analysis of the curvature and the influence of different sources. The strain through lattice mismatch does not differ significantly between the samples, since they are all consisting of the same sequence of material (AlN on Si, AlGaN on AlN, GaN on AlGaN and interlayers of AlN). Thus for simplicity this strain through lattice mismatch is considered equal for all samples.

The strain through thermal mismatch can be calculated through equation A.2. The temperature difference upon cool down is also recorded by temperature sensors near the surface and the difference in TEC is known. Again, through equation A.5 this strain value can be converted to a curvature value. In order to do so the thickness of the film is needed; a parameter that unfortunately is not recorded by EpiCurve TT. The sensor does record the Fabry-Pérot oscillations however, which can be translated to a growth rate (as explained in section A.2.3). Using the step code (a parameter that keeps track of which step of the growth process is carried out) one can approximate the growth time, which can be multiplied by the growth rate to give a layer thickness. Per step in the growth process also the growth material (Gan, AlGaN or AlN) changes and therefore the difference in thermal expansion coefficient. The evolution of the curvature is then approximated as a sum of the thermal mismatch strain per step in the recipe:

$$\kappa_{tm} = 15.67 \cdot 10^3 \sum\nolimits_{layer} GR_{layer}\, dt_{layer}\, (\alpha_{layer} - \alpha_{substrate}) \tag{A.13}$$

Even though the change in curvature upon cool down should be the same for all structures (since they consist of the same layer sequences with the same difference in TEC), the different growth rates recorded give a slight difference (4%) in this curvature attributed to thermal mismatch between the different samples.

A.3 Results

Figure A.5 shows the curvature measured during growth of three different sample runs. The curvature is an average over multiple wafers in the same run. The arrows at the right side represent the average of the (temperature corrected) bow measurements done with the Flatmaster ex-situ and show great accordance with the curvature measured by EpiCurve TT. From this graph one can see a clear distinction between the high pressure and low pressure samples. Up until 2.5 hours of growth (representing the growth of the graded buffer layers) the curvature of all samples evolves in a similar

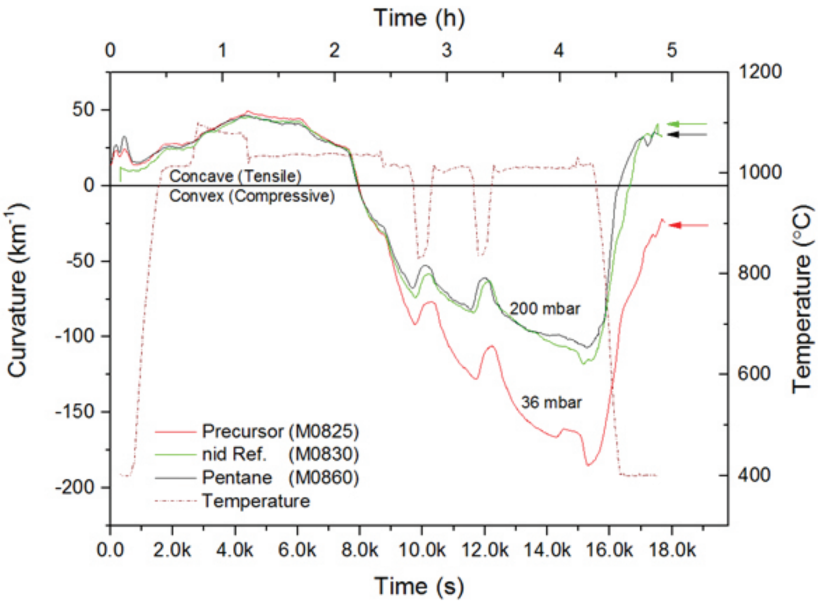

FIGURE A.5: The evolution of the wafer curvature over time for the different samples. The arrows at the right hand side mark the (converted and adjusted) bow values measured ex-situ. N.B. the range of the temperature sensor, which has a lower limit of 400°C. From the recipe a final temperature of about 100°C is found. The temperature graph is taken from the pentane doped (M0860) run. This makes it applicable to all 200 mbar samples, but is a little higher than the temperature for the 36 mbar run.

fashion. Afterwards (at the start of either doped or undoped GaN) the low pressure sample grows to a significantly more negative curvature. When at cool down all samples undergo the same increase in curvature this makes the low pressure samples end up with a negative curvature (i.e. convex and compressively strained), whereas the high pressure samples end up at positive curvatures (i.e. concave and tensile strained). Although all samples end up with a similar acceptable absolute value of curvature, within ±56 km^{-}1, a negative curvature is preferred. Positive curvature namely implicates tensile strained layers, leaving the structure susceptible to cracks.

The steep increase of the curvature after approximately 4.5 hours is the infamous tensile strain caused by cool down (as can be seen in the dotted curve representing the temperature). This increase in curvature can be measured and then compared to the

TABLE A.1: Measured and calculated changes in curvature $d\kappa$ upon cool down

Sample	$d\kappa$ **from graph**	$d\kappa$ **from calculation**	$\Delta d\kappa$
M0825	161	168	7
M0830	159	169	10
M0831	150	175	25
M0860	143	176	33

theoretical value calculated using equation B.11. The result of these measurements and calculations are presented in table A.1. One can see from this table that the measured and calculated values for run M0825 and M0830 are quite close, whereas the values for M0860 and M0831 are deviating significantly more. When looking at equation B.9 and B.10, and keeping in mind that the contribution due to lattice mismatch is considered equal for all runs, this suggests that there is a larger contribution of strain relaxation due to defects in these latter runs. This is confirmed, as mentioned in section 3.2.2, by the existence of cracks in these runs, whereas there are no cracks observed in M0825 and M0830.

Appendix B

Proofs

In this appendix mathematical proofs of formulas introduced in other sections of the thesis are presented.

B.1 Facet angle of a V-pit

In section 2.4.1 the facet angle of a V-pit with s_m-planes is introduced through equation 2.8. This facet angle α can be expressed in lattice parameters a and c. Figure B.1A shows a side view of an s_m-plane. The facet angle α between the two vectors and angle β between the vector and the plane sum up to 90°, the definition of the vector of a plane. This angle β is found again in the triangle bound by solid lines (through the alternate interior angle theorem). This triangle is bound by atoms, of which the distance between the atoms is c and x. Angle α can be found in this triangle again, by definition of a right triangle, and can be expressed as:

$$\alpha = tan^{-1}\frac{c}{x} \tag{B.1}$$

Figure B.1B represents a top view of the situation, in which the blue square represents the s_m-plane. The in-plane lattice parameters of the hexagonal structure are all the same (length a) and therefore the horizontal component of the s_m-plane equals a vector x, pointing from the central atom of the hexagon to the middle of a line between two neighboring atoms at the edge of the hexagon. The length of vector x follows from

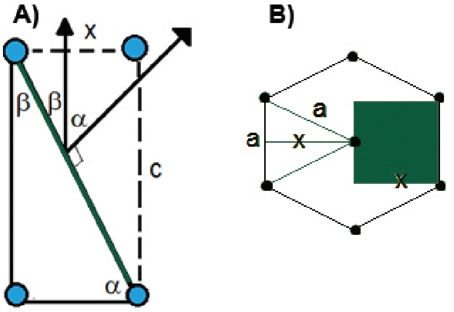

Figure B.1: A) side view and B) top view of an s$_m$-plane. α is the facet angle, β its complementary angle, x is the horizontal component of the vector connecting to neighboring atoms and c the out-of-plane lattice constant

simple geometry, knowing the angles of an equilateral triangle are 60°:

$$x = tan\,60° \cdot \frac{a}{2} = \frac{\sqrt{3}\,a}{2} \tag{B.2}$$

This can be combined with equation B.1 to finally hold:

$$\alpha = tan^{-1}\left(\frac{2\,c}{\sqrt{3}\,a}\right) \tag{B.3}$$

B.2 Measurement of facet angle of V-pit

In order to determine the facet angle of a V-pit, the depth of the pit can be measured by tilting the sample (illustrated in figure B.2A), as mentioned in section 4.3.1 and expressed in equation 4.1. The depth of the pit follows from the apparent shift of the center dy. The line depicting the depth Y is tilted by an angle equal to the tilt angle γ. The depth can then be calculated by relating the tilt angle to the apparent shift of the center through:

$$Y = \frac{dy}{sin\,\gamma} \tag{B.4}$$

Similar to proof B.1 one can proof that the facet angle α can be found in a triangle bound by the facet, the depth of the pit and half the diameter of the pit (see figure

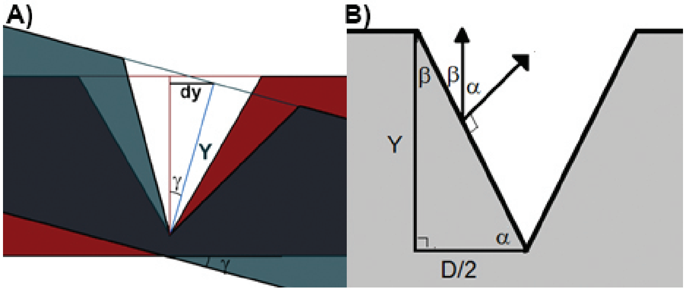

FIGURE B.2: Side view of A) a tilted and B) an untilted V-pit. γ is the tilt angle, dy the apparent shift of the center of the pit, Y the deduced pit depth, α is the facet angle, β its complementary angle and $D/2$ half the pit diameter.

B.2B). Therefore the facet angle can be expressed as:

$$\alpha = tan^{-1}\left(\frac{2\,Y}{D}\right) \tag{B.5}$$

Combined with equation B.4 this gives:

$$\alpha = tan^{-1}\left(\frac{2\;dy}{D\;sin\,\gamma}\right) \tag{B.6}$$

B.3 Relationship between curvature and bow

In section A.2.1, equation A.6 is used to convert a value for the bow of a wafer into a value for the curvature. In the figure B.3 R_w is the radius of the wafer, b is the bow of

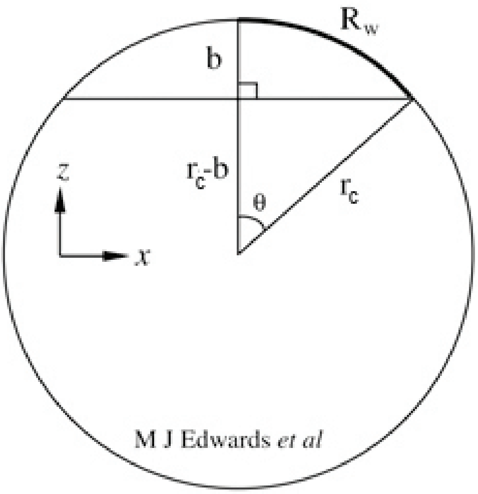

FIGURE B.3: Radius of curvature and bow for a curved wafer. R_w is the radius of the wafer, b is the bow of the wafer and r_c the radius of curvature. Adapted from Edwards et al the wafer and r_c the radius of curvature. The angle Θ equals R_w/r_c by definition of a central angle. Then one can see:

$$r_c - b = r_c \cdot cos\,\Theta \tag{B.7}$$

$$b = r_c - r_c \cdot cos\,\Theta = r_c\,(1 - cos\,\Theta) \tag{B.8}$$

$$b = r_c\left(1 - cos\left(\frac{R_w}{r_c}\right)\right) \tag{B.9}$$

Because of the radius r_c appearing both in the cosine and in front of the cosine, this equation cannot be solved explicitly for r_c. To avoid this problem, one can replace the cosine by a Taylor series. In the first order this gives:

$$cos\,\Theta = 1 - \frac{\Theta^2}{2} \tag{B.10}$$

Inserting this in the previous equation one gets:

$$b = r_c\left(1 - \left(1 - \frac{R_w^2}{2r_c^2}\right)\right) = r_c\,\frac{R_w^2}{2r_c^2} = \frac{R_w^2}{2r_c} \tag{B.11}$$

Knowing that the curvature κ equals the reciprocal of the radius of curvature r_c and the radius of the wafer R_w is half the wafer diameter ($D_w/2$), one gets:

$$b = \frac{\kappa \cdot D_w^2}{8} \tag{B.12}$$

which can be readily inverted to:

$$\kappa = \frac{8\,b}{D_w^2} \tag{B.13}$$

The minus sign is then introduced to sort out the definition; a concave wafer has negative bow and positive curvature:

$$\kappa = -\frac{8\,b}{D_w^2} \tag{B.14}$$

Bibliography

[1] Kazukiyo Joshin, Toshihide Kikkawa, Satoshi Masuda, and Keiji Watanabe. Outlook for GaN HEMT Technology. *FUJITSU Sci. Tech. J.*, 50(1):138–143, 2014.

[2] Umesh K. Mishra, Primit Parikh, and Yi-Feng Wu. AlGaN/GaN HEMTs: An overview of device operation and applications. *Proceedings of the IEEE*, 90(6): 1022–1031, 2002.

[3] Ian Poole. HEMT, High Electron Mobility Transistor Tutorial. n.d. *Retrieved October 12, 2015*, from www.radio-electronics.com.

[4] Umesh K. Mishra, L. Shen, T.E. Kazior, and Yi-Feng Wu. GaN-Based RF Power Devices and Amplifiers. *Proceedings of the IEEE*, 96(2):287–305, 2008.

[5] The 2014 Nobel Prize in Physics - Press Release. October 7 2014. *Retrieved October 12, 2015*, from www.nobelprize.org.

[6] Miguel Angel Caro Bayo. *Theory of elasticity and electric polarization effects in the group-III nitrides.* PhD thesis, 2013.

[7] M. Moram and M.E. Vickers. X-ray diffraction of III-nitrides. *Reports on progress in physics*, 72(3), 2009.

[8] I. Verguftman and J.R. Meyer. Band parameters for nitrogen-containing semiconductors. *Journal of Applied Physics*, 94(6):3675–3696, 2003.

[9] Taek Lim. *Ternre und quaternre Barrierenmaterialen fr nitridische Heterostruktur-Feldeffekttransistoren.* PhD thesis, 2011.

[10] L. Liu and J.H. Edgar. *Materials Science and Engineering*, R37(61), 2002.

[11] M. Stutzmann, O. Ambacher, M. Eickhoff, U. Karrer, A. Lima Pimenta, R. Neuberger, J. Schalwig, R. Dimitrov, P.J. Schuck, and R.D. Grober. Playing with Polarity. *Phys. Status Solidi B*, 228(2):505–512, 2001.

[12] E. Bahat-Treidel. *GaN-Based HEMTS for High Voltage Operation: Design, Technology and Characterization.* PhD thesis, 2012.

[13] R.L. Anderson. Germanium-Gallium Arsenide Heterojunctions. *IBM Journal of Research and Development*, 4(3):283–287, 1960.

[14] O. Ambacher, J. Majewski, C. Miskys, A. Link, M. Hermann, M. Eickhoff, M. Stutzmann, F. Bernardini, V. Fiorentini, V. Tilak, B. Schaff, and L.F. Eastman. Pyroelectric properties of Al(In)GaN/GaN hetero- and quantum well structures. *Journal of Physics: Condensed Matter*, 14(13):3399–3434, 2002.

[15] O. Ambacher, J.A. Smart, J.R. Shealy, N.G. Weimann, and K. Chu. Two-dimensional electron gasses induced by spontaneous and piezoelectric polarization charges in N- and Ga-face AlGaN/GaN heterostructures. *Journal of Applied Physics*, 85(6):3222–3233, 1999.

[16] R.J. Trew, G.L. Bilbro, W. Kuang, Y. Liu, and H. Yin. Microwave AlGaN/GaN HFETs. *IEEE Microwave Magazine*, 6(1):56–66, 2005.

[17] Tanvir Hasan. *Mechanism and Suppression of Current Collapse in AlGaN/GaN High Electron Mobility Transistors.* PhD thesis, 2013.

[18] Anthony C. Jones and Michael L. Hitchman. *Chemical Vapour Deposition: Precursors, Processes and Applications*, chapter 1, pages 5–7. Royal Society of Chemistry, 2009.

[19] Debasis Sengupta, Sandip Mazumder, William Kuykendall, and Samuel A. Lowry. Combined ab initio quantum chemistry and computational fluid dynamics calculations for prediction of gallium nitride growth. *Journal of Crystal Growth*, 279: 369–382, 2005.

[20] G.B. Stringfellow. *Organomettalic vapor phase epitaxy: theory and practice.* Academic Press, Boston, 1989.

[21] Frank Stefan Habel. *Methoden zur Defektreduktion von Galliumnitrid-substraten und -Quasisubstraten.* PhD thesis, 2006.

[22] Kai Fu. *Growth Dynamics of Semiconductor Nanostructures by MOCVD.* PhD thesis, 2009.

[23] Rinku P. Parikh and Raymond A. Adomaitis. An overview of gallium nitride chemistry and its effect on reactor design: Application to a planetary radial-flow CVD system. *Journal of Crystal Growth*, 286:259–278, 2006.

[24] Evgeniya Dontsova. *Understanding of edge and screw dislocations in nanostructures by modeling and simulations.* PhD thesis, 2013.

[25] J.R. Dorfman and A.J. Faller. Jan Burgers. *Physics Today*, 35(1), 1982.

[26] J.L. Weyher, S. Lazar, L. Macht, Z. Liliental-Weber, R.J. Molnar, S. Mller, V.G.M. Sivel, G. Nowak, and I. Grzegory. Orthodox etching of HVPE-grown GaN. *Journal of Crystal Growth*, 305:384–392, 2007.

[27] F.C. Frank. Capillary Equilibria of Dislocated Crystals. *Acta Crystallographica*, 4:497–501, 1951.

[28] John E Northrup, Jrg Neugebauer, and L.T. Romano. Inversion Domain and Stacking Mismatch Boundaries in GaN. *Physical Review Letters*, 77(1):103–106, 1996.

[29] Chihiro Iwamoto, Xu-Qiang Shen, Hajime Okumura, Hirofumi Matsuhata, and Yuuichi Ikuhara. Structure Analysis of GaN Thin Film with Inversion Domains by High Voltage Atomic Resolution Microscopy. *MAterials Transactions*, 43(7): 1542–1546, 2002.

[30] S. Lawrence Selvaraj, Takaaki Suzue, and Takashi Egawa. Influence of Deep Pits on the Breakdown of Metalorganic Chemical Vapor Deposition Grown AlGaN/GaN High Electron Mobility Transistors on Silicon. *Applied Physics Express*, 2, 2009.

[31] Pum Chian Khai, Takaaki Suzue, Yusuke Sakai, S. Lawrence Selvaraj, Takashi Egawa, and Takashi Jimbo. Correlation between growth pits, optical and structural properties of AlGaN/GaN high-electron-mobility transistors on 4” silicion substrate. *Phys. Status Solidi*, C7(7-8):1949–1951, 2010.

[32] Mi-Hyang Sheen, Sung-Dae Kim, Jong-Hwan Lee, Jong-In Shim, and Young-Woon Kim. V-pits as Barriers to Diffusion of Carriers in InGaN/GaN Quantum Wells. *Journal of Electronic Materials*, (to be published), 2015.

[33] A. Hangleiter, F. Hitzel, C. Netzel, D. Fuhrmann, U. Rossow, G. Ade, and P. Hinze. Suppression of Nonradiative Recombination by V-Shaped Pits in GaIn-N/GaN Quantum Wells Produces a Large Increase in the Light Emission Efficiency. *Physical Review Letters*, 95(127402), 2005.

[34] Chiao-Yun Chang, Heng Li, Yang-Ta Shih, and Tien-Chang Lu. Manipulation of nanoscale V-pits to optimize internal quantum efficiency of InGaN multiple quantum wells. *Applied Physics Letters*, 106, 2015.

[35] S. Schwaiger, S. Metzner, T. Wunderer, I. Argut, J. Thalmair, F. Lipski, M. Wieneke, J. Blsing, F. Bertram, J. Zweck, and A. Krost. Growth and coalescence behavior of semipolar (11-22) GaN on pre-structured r-plane sapphire substrates. *Phys. Status Solidi B*, 248(3):588–593, 2011.

[36] Z.L. Miao, T.J. Yu, F.J. Xu, J. Song, C.C. Huang, X.Q. Wang, Z.J. Yang, G.Y. Zhang, X.P. Zhang, D.P. Yu, and B. Shen. The origin and evolution of V-defects in InxAl1-xN epilayers grown by metalorganic chemical vapor deposition. *Applied Physics Letters*, 95(231909), 2009.

[37] Jaekyn Kim, Joosung Kim, Youngjo Tak, Suhee Chae, Jun-Youn Kim, and Youngsoo Park. Effect of V-Shaped Pit Size on the Reverse Leakage Current of InGaN/-GaN Light Emitting Diodes. *IEEE Electron Device Letters*, 34(11):1409–1411, 2013.

[38] Z. Liliental-Weber, Y. Chen, S. Ruvimov, and J. Washburn. Formation Mechanism of Nanotubes in GaN. *Physical Review Letters*, 79(15):2835–2838, 1997.

[39] P. Vennéguès, B. S. Diaby, H. Kim-Chauveau, L. Bodiou, H. P D Schenk, E. Frayssinet, R. W. Martin, and I. M. Watson. Nature and origin of V-defects present in metalorganic vapor phase epitaxy-grown (In xAl 1-x)N layers as a function of InN content, layer thickness and growth parameters. *Journal of Crystal Growth*, 353, 2012.

[40] Vladislav Voronenkov, Natalia Bochkareva, Ruslan Gorbunov, Philipp Latyshev, Yuri Lelikov, Yury Rebane, Alexander Tsyuk, Andrey Zubrilov, and Yuri Shreter. Nature of V-Shaped Defects in GaN. *Japanese Journal of Applied Physics*, 52 (08JE14), 2013.

[41] Lin Zhou, Martha R. McCartney, David J. Smith, Anas Mouti, E. Feltin, J.F. Carlin, and N. Grandjean. Observation of dodecagon-shape V-defects in GaN/AlInN multiple quantum wells. *Applied Physics Letters*, 97(161902), 2010.

[42] Junyong Kang, Shin Tsunekawa, Bo Shen, Zhenhong Mai, Chaoying Wang, Toshihid Tsuru, and Atsuo Kasuya. Nanopipes in undoped AlGaN epilayers. *Journal of Crystal Growth*, 229:58–62, 2001.

[43] Fei Ma and Ke-Wei Xu. Using dangling bond density to characterize the surface energy of nanomaterials. *Surface and Interface Analysis*, 39:611–614, 2007.

[44] Hong Li, Lutz Geelhaar, Henning Riechert, and Claudia Draxl. Computing Equilibrium Shapes of Wurtzite Crystals: The Example of GaN. *Physical Review Letters*, 115(085503), 2015.

[45] J. Elsner, R. Jones, M. Haugk, R. Gutierrez, Th. Frauenheim, M.I. Heggie, S. berg, and P.R. Briddon. Effect of oxygen on the growth of (10-10) GaN surfaces: The formation of nanopipes. *Applied Physics Letters*, 73(24):3530–3532, 1998.

[46] Th. Kehagias, G.P. Dimitrakopulos, J. Kioseoglou, H. Kirmse, C. Giesen, M. Heuken, A. Georgakilas, W. Neumann, Th. Karakostas, and Ph. Komninou. Indium migration paths in V-defects on InAlN grown by metal-organic vapor phase epitaxy. *Applied Physics Letters*, 95(071905), 2009.

[47] John. E. Northrup and Jrg Neugebauer.

[48] K. Hiramatsu, K. Nishiyama, A. Motogaito, H. Miyake, Y. Iyechika, and T. Maeda. Recent progress in selective area growth and epitaxial lateral overgrowth of III-nitrides: effects of reactor pressure in MOVPE growth. *Phys. Status Solidi*, A176: 535–543, 1999.

[49] J.R. Yang, W.C. Li, H.L. Tsai, J.T. Hsu, and M. Shiojiri. Electron microscopy investigations of V defects in multiple InGaN/GaN quantum wells and InGaN quantum dots. *Journal of Microscopy*, 237(3):275–281, 2010.

[50] Kwang Suk Son, Dong Gyu Kim, H. K. Cho, Kyuhan Lee, Sunwoon Kim, and Keunseop Park. Formation of V-shaped pits in GaN thin films grown on high temperature GaN. *Journal of Crystal Growth*, 261:50–54, 2004.

[51] Huanyou Wang, Xianchun Wang, Qiaolai Tan, and Xiaohua Zeng. V-defects formation and optical properties of InGaN/GaN multiple quantum well LED grown on patterned sapphire substrate. *Materials Science in Semiconductor Processing*, 29, 2013.

[52] Structural origin of V-defects and correlation with localized excitonic centers in InGaN/GaN multiple quantum wells. *Applied Physics Letters*, 72(6):692–694, 1998.

[53] B. Pecz, Zs. Makkai, M. a. di Forte-Poisson, F. Huet, and R. E. Dunin-Borkowski. V-shaped defects connected to inversion domains in AlGaN layers. *Applied Physics Letters*, 78(11):1529, 2001.

[54] H.K. Cho, J.Y. Lee, G.M. Yang, and C.S. Kim. Formation mechanism of V defects in the InGaN/GaN multiple quantum wells grown on GaN layers with low threading dislocation density. *Applied Physics Letters*, 79(2):215–217, 2001.

[55] V.N. Bessolov, E.V. Konenkova, A.V. Zubkova, A.V. Osipov, T.A. Orlova, S.N. Rodin, and S.A. Kukushkin. The mechanism of fomration of structural V-defects in polar and semipolar epitaxial GaN films synthesized on SiC/Si(111) and SiC/Si(100) heterostructures. *Materials Physics and Mechanics*, 21:266–274, 2014.

[56] I.Y. Knoke, P. Berwian, E. Meissner, J. Friedrich, H.P. Strunk, and G. Mller. Selectiveethcing of dislocations in GaN grown by low-pressure solution growth. *Journal of Crystal Growth*, 312:3040–3045, 2010.

[57] N. Cabrera and M.M. Levine. *Philosophical Magazine*, 1(5):450–458, 1956.

[58] T.L. Song. Strain relaxation due to V-pit formation in $\mathrm{In}_x\mathrm{Ga}_{1-x}\mathrm{N}$/GaN epilayers grown on sapphire. *Journal of Applied Physics*, 98, 2005.

[59] Yi-Feng Wu, David Kapolnek, James P. Ibbetson, Primit Parikh, Bernd P. Keller, and Umesh K. Mishra. Very-High Power Density AlGaN/GaN HEMTs. *IEEE Transactions on electronic devices*, 48(3):586–590, 2001.

[60] Hans Lth. chapter 3. Springer-Verlag Berlin Heidelberg, 2001.

[61] Ashutosh Sagar and R.M. Feenstra. *Growth of GaN on porous SiC by molecular beam epitaxy.* Wiley, West Sussex, 2008.

[62] S.A. Kukushkin, A.V. Osipov, V.N. Bessolov, B.K. Medvedev, V.K. Nevolin, and K.A. Tcarik. Substrates for epitaxy of gallium nitride: new materials and techniques. *Reviews on advanced materials science*, 17:1–32, 2008.

[63] J.R. Shealy, V. Kaper, V. Tilak, T. Prunty, J.A. Smart, B. Green, and L.F. Eastman. An AlGaN/GaN high-electron-mobility transistor with an AlN sub-buffer layer. *Journal of Physics: Condensed Matter*, 14:3499–3509, 2002.

[64] A. Dadgar, F. Schulze, M. Wienecke, A. Gadanecz, J. Blsing, P. Veit, T. Hempel, A. Diez, J. Christen, and A. Krost. Epitaxy of GaN on silicon - impact of symmetry and surface reconstruction. *New Journal of Physics*, 9(389), 2007.

[65] P.R. Hageman, S. Haffouz, A. Grzegorczk, V. Kirilyuk, and P.K. Larsen. Growth of GaN epilayers on Si(111) substrates using multiple buffer layers. *Materials Research Society Symposium Proceedings*, 693:1–6, 2002.

[66] Jonathan G. Felbinger, M.V.S. Chandra, Yunju Sun, Lester F. Eastman, John Wasserbauer, Firooz Faili, Dubravko Babic, Danicel Francis, and Felix Ejeckham. Comparison of GaN HEMTs on Diamond and SiC Substrates. *IEEE Electron Device Letters*, 28(11):948–950, 2007.

[67] H. Amano, N. Sawaki, I. Akasaki, and Y. Toyoda. Metalorganic vapor phase epitaxial growth of a high quality GaN film using an AlN buffer layer. *Applied Physics Letters*, 48(5):353–355, 1986.

[68] Alois Krost and Armin Dadgar. GaN-based optoelectronics on silicon substrates. *Materials Science and Engineering B*, 93:77–84, 2002.

[69] A. Able, W. Wegschieder, K. Engl, and J. Zweck. Growth of crack-free GaN on Si(111) with graded AlGaN buffer layers. *Journal of Crystal Growth*, 276:415–418, 2005.

[70] Y. Yang, P. Xiang, M. Liu, W. Chen, Z. He, X. Han, Y. Ni, F. Yang, Y. Yao, Z. Wu, Y. Liu, and B. Zhang. Effect of compositionality graded AlGaN buffer layer grown by different functions of trimethylaluminum flow rates on the properties of GaN on Si(111) substrates. *Journal of Crystal Growth*, 376:23–27, 2013.

[71] B. Leung, J. Han, and Q. Sun. Strain relaxation and dislocation reduction in AlGaN step-graded buffer for crack-free GaN on Si(111). *Phys. Status Solidi C*, 11(3-4):437–411, 2014.

[72] X. Yu, J. Ni, Z. Li, J. Zhou, and C. Kong. Reduction in leakage current in AlGaN/GaN HEMT with three Al-containing step-graded AlGaN buffer layers on silicon. *Japanese Journal of Applied Physics*, 53(051001), 2014.

[73] Tingkai Li, Michael Mastro, and A. Dadgar. chapter 4. CRC Press, 2011.

[74] J. Gleize, F. Demangeot, J. Frandon, M.A. Renucci, F. Widmann, and B. Daudin. Phonons in a strained hexagonal GaN-AlN superlattice. *Applied Physics Letters*, 74(5):703–705, 1999.

[75] H. Amano, M. Iwaya, T. Kashima, M. Katsuragawa, I. Akasaki, J. Han, S. Hearne, J.A. Floro, E. Chason, and J. Figiel. Stress and Defect Control in GaN Using Low Temperature Interlayers. *Japanese Journal of Applied Physics*, 37:1540–1542, 1998.

[76] A.F. Wright. Substitutional and interstitial carbon in wurtzite GaN. *Journal of Applied Physics*, 92(2575), 2002.

[77] J.B. Webb, H. Tang, S. Rolfe, and J.A. Bardwell. Semi-insulating C-doped GaN and high mobility AlGaN/GaN heterostructures grown by ammonia molecular beam epitaxy. *Applied Physics Letters*, 75(7):953–955, 1999.

[78] J.L. Lyons, A. Janotti, and C.G. Van de Walle. Carbon impurities and the yellow luminescence in GaN. *Applied Physics Letters*, 97(152108), 2010.

[79] J.G. Simmons and G.W. Taylor. Nonequilibrium Steady-State Statistics and Associated Effects for Insulators and Semiconductors Containing an Arbitray Distribution of Traps. *Physical Review B*, 4(2):502–511, 1971.

[80] H. Tang, J.B. Webb, J.A. Bardwell, S. Raymond, J. Salzman, and C. Uzan-Saguy. Properties of carbon-doped GaN. *Applied Physics Letters*, 78(6):757–759, 2001.

[81] J. Salzman, C. Uzan-Saguy, R. Kalish, V. Richter, and B. Meyler. Thermally activated electrical conductivity in thin GaN epitaxial films. *Applied Physics Letters*, 76(11):1431–1433, 2000.

[82] M. Fehrer, S. Einfeldt, U. Birkle, T. Gollnik, and D. Hommel. Impact of defects on carrier transport in GaN. *Journal of Crystal Growth*, 189-190:763–767, 1998.

[83] J.F. Du, Z. Bai, K. Ma, and Q. YU. Influence of Trap State Effects on Buffer Leakage Current and Breakdown Voltage in Nano-Channel AlGaN/GaN DHFETs. *Nanoscience and Nanotechnology Letters*, 6(9):794–797, 2014.

[84] Jr-Tai Chen, Urban Forsberg, and Erik Janzen. Impact of residual carbon on two-dimensional electron gas properties in AlxGa1-xN/GaN heterostructure. *Applied Physics Letters*, 102(193506), 2013.

[85] P.B. Klein, S.C. Binari, K. Ikossi, A.E. Wickenden, D.D. Koleske, and R.L. Henry. Current collapse and the role of carbon in AlGaN/GaN high electron mobility transistors grown by metalorganic vapor-phase epitaxy. *Applied Physics Letters*, 79(21):3527–3529, 2001.

[86] H.T. Lam and J.M. Vohs. Surface reactions of thrimethylgallium on MOVPE-grown GaN(0001). *Surface Science*, 426(2):199–211, 1999.

[87] Jack H Lunsford. Catalytic conversion of methane to more useful chemicals and fuels: a challenge for the 21st century. *Catalysis Today*, 63(2-4):165–174, 2000.

[88] Jian-Li Zhang, Jun-Lin Liu, Yong Pu, Wen-Qing Fang, Meng Zhang, and Jiang Feng-Yi. Effects of Carrier Gas on Carbon Incorporation in GaN. *Chinese Physics Letters*, 31(3), 2014.

[89] D.D. Koleske, A.E. Wickenden, R.L. Henry, and M.E. Twigg. Influence of MOVPE growth conditions on carbon and silicon concentrations in GaN. *Journal of Crystal Growth*, 242:55–69, 2002.

[90] C. Lee, L. Witkowski, H.-Q. Tserng, P. Saunier, R. Birkhahn, D. Olson, D. Olson, G. Munns, S. Guo, and B. Albert. Effects of AlGaN/GaN HEMT structure on RF reliability. *Electronics Letters*, 41(3), 2005.

[91] D.W. Gotthold, S.P. Guo, R. Birkhahn, B. Albert, D. Florescu, and B. Peres. Time-Dependent Degradation of AlGaN/GaN Heterostructures Grown on Silicon Carbide. *Journal of Electronic Materials*, 33(5):408–411, 2004.

[92] Ponky Ivo, Arkadiusz Glowacki, Reza Pazirandeh, E. Bahat-Treidel, Richard Lossy, Joachim Wrfl, Christian Boit, and Gunther Trnkle. Influence of GaN cap

on robustness of AlGaN/GaN HEMTs. *Reliability Physics Symposium, 2009 IEEE International*, pages 71–75, 2009.

[93] Jungwoo Joh and Jess A. del Alamo. Critical Voltage for Electrical Degradation of GaN High-Electron Mobility Transistors. *2008*, 29(4):287–289, 2008.

[94] Yoshio Honda, Norifumi Kameshiro, Masahito Yamaguchi, and Nobuhiko Sawaki. Growth of (1-101) GaN on 7-degree off-oriented (001)Si substrate by selective MOVPE. *Journal of Crystal Growth*, 242:82–86, 2002.

[95] A.E. Romanov, E.C. Young, Feng Wu, Anurag Tyagi, Gallinat. C.S., S. Nakamura, S.B. DenBaars, and J.S. Speck. Basal plane misfit dislocations and stress relaxation in III-nitride semipolar heteroepitaxy. *Journal of Applied Physics*, 109, 2011.

[96] T. Tanikawa, T. Hikosaka, Yoshio Honda, Masahito Yamaguchi, and N. Sawaki. Growth of semi-polar (11-22)GaN on a (113)Si substrate by selective MOVPE. *Phys. Status Solidi C*, 5(9):2966–2968, 2008.

[97] B. Beaumont, S. Haffouz, and P. Gibart. Magnesium induced changes in the selective growth of GaN by metalorganic vapor phase epitaxy. *Applied Physics Letters*, 72(8):921–923, 1998.

[98] H. Lahrèche, P. Vennéguès, B. Beaumont, and P. Gibart. Growth of high-quality GaN by low-pressure metal-organic vapour phase epitaxy (LP-MOVPE) from 3D islands and lateral overgrowth. *Journal of Crystal Growth*, 205:245–252, 1999.

[99] Qian Sun, Christopher D. Yerino, Benjamin Leung, Jung Han, and Michael E. Coltrin. Understanding and controlling heteroepitaxy with the kinetic Wulff plot: A case study with GaN. *Journal of Applied Physics*, 110(5), 2011.

[100] F. Brunner, A. Knauer, T. Schenk, M. Weyers, and J.-T. Zettler. Quantitative analysis of in situ wafer bowing measurements for III-nitride growth on sapphire. *Journal of Crystal Growth*, 310:2432–2438, 2008.

[101] C.J. Glassbrenner and Glen A. Slack. Thermal Conductivity of Silicon and Germanium from 3K to the Melting Point. *Physical Review*, 134(4A):1058–1069, 1964.

[102] Nicola Rollbhler. *Untersuchung der Verspannung von Galliumnitrideschichten auf Siliziumsubstraten.* PhD thesis, 2011.

[103] R. Clos, A. Dadgar, and A. Krost. Wafer curvature in the nonlinear deformation range. *Phys. Status Solidi a*, 201(11):75–78, 2004.

[104] Rolf Aidam, Elke Diwo, Nicola Rollbhler, Lutz Kirste, and Fouad Benkhelifa. Strain control of AlGaN/GaN high electron mobility transistor structures on silicon (111) by plasma assisted molecular beam epitaxy. *Journal of Applied Physics*, 111(11), 2012.

[105] N a Ochoa, G Mendiola, and J E a Landgrave. Flatness measurement using a grazing incidence interferometer. *Revista Mexicana De Fisica*, 53(1):66–71, 2007.

[106] Hideo Aida, Dong S. Lee, Mikhail Belousov, and Kazuhiko Sunakawa. Effect of Initial Bow of Sapphire Substrate on Substrate Curvature during InGaN Growth Stage of Light Emitting Diode Epitaxy. *Japanese Journal of Applied Physics*, 51: 1–5, 2012.